Drag Coefficient Constraints for Space Weather Observations in the Upper Thermosphere

Valerie Bernstein[1,2] **and Marcin Pilinski**[2,3]

[1]Ann and H.J. Smead Department of Aerospace Engineering Sciences, University of Colorado Boulder, 3775 Discovery Drive, Boulder, Colorado, 80303
[2]Laboratory for Atmospheric and Space Physics, 1234 Innovation Drive, Boulder, Colorado, 80303
[3]Space Weather Technology, Research, and Education Center, University of Colorado Boulder, 3775 Discovery Drive, Boulder, Colorado, 80303

Key Points:

- Drag coefficient errors lead to altitude-dependent biases in thermospheric densities
- Drag coefficient model assumptions are constrained by evaluating multi-satellite density consistency
- Aerodynamic drag modeling is improved near 500 km by assuming incomplete momentum accommodation

Corresponding author: Valerie Bernstein, `valerie.bernstein@colorado.edu`

Abstract

The space weather research community relies heavily on thermospheric density data to understand long-term thermospheric variability, construct assimilative, empirical, and semi-empirical global atmospheric models, and validate model performance. One of the challenges in resolving accurate thermospheric density datasets from satellite orbital drag measurements is modeling appropriate physical aerodynamic drag force coefficients. The drag coefficient may change throughout the thermospheric environment due to model dependencies on composition and altitude. As such, existing drag coefficient model errors may be altitude and solar cycle dependent, with greater errors at higher altitudes around 500 km near the oxygen-to-helium transition region. This can lead to errors in orbit-derived density datasets and models. In this paper, inter-satellite density comparisons at ∼500 km are evaluated to constrain drag coefficient modeling assumptions. Density consistency results indicate that drag coefficient models with incomplete energy and momentum accommodation produce the most consistent densities, while the standard diffuse modeling approach may not be appropriate at these altitudes. Models with momentum accommodation between 0.5 - 0.9 and energy accommodation between 0.83 - 0.96 may be the most appropriate at upper thermospheric altitudes. Modeling drag coefficients with diffuse gas-surface interactions could lead to errors in derived density of ∼25% and in-track satellite orbit prediction uncertainty during solar maximum conditions on the order of hundreds of meters.

Plain Language Summary

The Earth's upper atmosphere exerts forces on satellites that can change their paths. It is critical to understand how these atmospheric drag forces work in order to measure atmospheric variability and predict satellite orbital paths in an increasingly crowded near-Earth space. The atmospheric drag force depends on interactions between atmospheric particles and the surface of a satellite. Gas particles can impact a satellite surface and scatter in a variety of ways. Depending on the speed and direction of the scattered particles, the atmospheric drag force on a satellite can change. The appropriate type of scattering for atmospheric particles interacting with a satellite surface in orbit remains uncertain. In this work, the authors try to infer the nature of gas-surface scattering by comparing atmospheric densities derived from orbital changes measured for satellites of different shapes. The density comparisons suggest that standard assumptions about surface scattering in orbit may not be appropriate, but rather assuming scattering that is less random may be better at upper altitudes near and above 500 km. Assuming the wrong scattering physics could lead to errors in densities derived from satellite orbital data of ∼25% and satellite orbit prediction variations of 10s-100s of meters along the satellite track.

1 Introduction

Modeling accurate physical aerodynamic drag coefficients for satellites in orbit is critical for understanding atmospheric drag variability and maintaining space domain awareness in the Low Earth Orbit (LEO) environment. Drag coefficients (C_D) are used to calibrate density models and extract atmospheric density and wind information from on-orbit observations (Doornbos, 2012; Sutton et al., 2007; P. M. Mehta et al., 2017; March, Visser, et al., 2019). Furthermore, inferred wind speeds and directions are sensitive to even small changes in energy accommodation in C_D models (Ching et al., 1977). Accurate drag coefficients in orbit are also needed to improve satellite orbital lifetime estimates. The drag coefficient may change throughout the geospace environment due to model dependencies on composition and altitude. Drag coefficient models tend to diverge at altitudes above 400 km (Pilinski et al., 2013; Pardini et al., 2009), which is where there are greater uncertainties in gas-surface interaction assumptions.

Physical satellite drag coefficients are characterized by gas-surface interactions (GSIs) describing the dynamics of the energy and momentum exchange between an impinging atmospheric atom or molecule and a satellite surface. GSI models characterize the angular distribution and velocity of the reemitted gas particles. These reemitted particle distributions can be described as diffuse, specular, or quasi-specular, with varying energy and momentum accommodation at the satellite surface. GSI physical dynamics are expected to be dependent on surface roughness, cleanliness, composition, and temperature as well as incident gas composition, temperature, velocity, and angle.

GSI models are typically characterized by parameters that constrain the velocity and angular distribution of reemitted gas particles, the most fundamental of which are accommodation coefficient parameters. The accommodation coefficients that quantify the energy and momentum exchange between the molecules and the surface include the energy accommodation coefficient, α, and the normal and tangential momentum accommodation coefficients, σ_n and σ_t. The energy accommodation coefficient controls the amount of energy that the incident molecules lose upon reemission, as indicated by Eq. (1) (Wachman, 1962).

$$\alpha = \frac{E_i - E_r}{E_i - E_s} = \frac{T_i - T_r}{T_i - T_s} \tag{1}$$

In Eq. (1), E_i is the kinetic energy from incident molecules hitting the surface, E_r is the kinetic energy leaving the surface from reemitted molecules, and E_s is the energy that would be transported away from the surface from reemitted molecules in thermal equilibrium with the surface. T_i, T_r, and T_s are the kinetic temperatures corresponding to the kinetic energies described above, respectively.

The amount of energy transferred determines the velocity of the reflected molecules, so energy accommodation is related to the reemission velocity. If $\alpha = 0$, then $E_i = E_r$, and the incident molecules are reemitted with speeds equal to the incident relative speed between the atmosphere and the satellite. If $\alpha = 1$, then $E_r = E_s$, and the incident molecules are reemitted with slower speeds after having reached thermal equilibrium with the satellite surface. The energy accommodation coefficient is split into normal and tangential components in some models.

The momentum accommodation coefficient represents the change in momentum between the incident molecules and the reemitted molecules. The momentum accommodation coefficient is often separated into normal and tangential exchange components, as this choice is associated with better agreement between theoretical calculations and observations (Schaaf & Chambre, 1958).

$$\sigma_n = \frac{p_{i,n} - p_{r,n}}{p_{i,n} - p_{s,n}} \tag{2}$$

$$\sigma_t = \frac{p_{i,t} - p_{r,t}}{p_{i,t} - p_{s,t}} \tag{3}$$

In Eqs. (2) and (3), the subscripts n and t signify normal and tangential components. The incident momentum flux is given by p_i, the reemitted momentum flux is given by p_r, and p_s is the momentum flux from diffusely reemitted molecules in thermal equilibrium with the surface (Storch, 2002).

The normal and tangential momentum accommodation coefficients are related to the reemitted velocity distribution (Walker et al., 2014). Diffuse scattering occurs when both σ components are equal to unity. Specular scattering occurs when both σ components are equal to 0. When σ_n and σ_t are valued between 0 and 1, reemission is quasi-specular in nature. In general, larger momentum and energy accommodation leads to more diffusive scattering and smaller reflected velocities. Smaller momentum and energy accommodation coefficients yield more quasi-specular scattering.

Table 1. C_D Models and Parameters

C_D Model	Parameters	Reemitted Distribution Characteristics
Sentman	α	Diffuse
Schamberg	α, ν, ϕ_0	Diffuse, specular, or quasi-specular
CLL	σ_n, σ_t	Diffuse, specular, or quasi-specular with scattering kernels

A great deal of theoretical groundwork on GSI physics has been developed, with fundamental contributions in the 1960s laying the foundation for updated modeling frameworks today. Early efforts from Sentman (1961) proposed diffuse scattering with complete or near-complete energy accommodation. Schamberg's model (Schamberg, 1959) could vary the reemission angle via the parameter ν and the lobe width via the parameter ϕ_0 to achieve a wide range of diffuse, specular, and quasi-specular reemitted particle distributions. Advancements by Goodman (Goodman & Wachman, 1967), and more recently the body of work from Moe and Moe (K. Moe et al., 1972; M. M. Moe et al., 1993; K. Moe & Moe, 2005), consider the effect of surface contamination or cleanliness. This led to the implementation of variable energy accommodation coefficients based on surface coverage by adsorbed gas particles, particularly atomic oxygen. Diffuse reflection with variable or incomplete accommodation (DRIA) is the current predominant method for computing drag coefficients for satellites in LEO. Many recent approaches (Sutton et al., 2007; Doornbos, 2012; March, Visser, et al., 2019) select the most appropriate value for energy accommodation in a DRIA model based on data consistency metrics or other insights from orbital measurements. Following the work of Moe and Moe, Pilinski et al. (2013) implemented DRIA with Langmuir isotherm-based variable energy accommodation based on atomic oxygen number density in the Semi-Empirical Satellite Accommodation Model (SESAM). Recent interest in the quasi-specular scattering model which implements scattering kernels and allows for variable accommodation known as the Cercignani-Lampis-Lord (CLL) model (Cercignani & Lampis, 1971, 1997; Lord, 1991) marks a significant shift in the computation of aerodynamic drag coefficients. The CLL model moves away from fully diffuse scattering and the DRIA framework that has characterized much of the orbital drag coefficient modeling advancements since the 1960s. Walker et al. (2014) and P. M. Mehta et al. (2014) implemented the CLL model with variable Langmuir-based energy accommodation to achieve scattering with narrower angular distribution lobes. Table 1 provides a summary of the relevant foundational C_D models examined in this analysis, their corresponding GSI parameters, and achievable reemitted distribution characteristics.

1.1 Insights from Laboratory Molecular Beam Experiments

Historical, current, and near-future laboratory molecular beam experiments provide insight into and estimates of physical gas-surface interactions. Studies by Cook (1965) led to the widely-used fixed drag coefficient of 2.2. Historically, many studies have either relied on laboratory measurements from clean, pristine surfaces that likely do not fully represent in-orbit conditions or have not controlled for surface contamination leaving it difficult to apply the results to orbital environments. Quasi-specular scattering has been demonstrated for clean materials under ultra-high vacuum conditions at orbital velocity conditions (Murray et al., 2017).

Some laboratory experiments have provided insight into the ideas that 1) gas-surface interactions may depend on the incident angle between the flow and the satellite surface normal, and 2) different gas constituents may scatter in unique ways. There has been some work that supports the idea that energy and momentum accommodation coefficients are expected to be a function of incident angle and constituent mass. Goodman

and Wachman (1967) and Wachman (1962) derived a formula for energy accommodation as a function of the ratio of the mass of the incident molecule to the mass of the surface material based on lattice theory and experimental data.

In general, laboratory experiments investigating helium scattering have concluded that helium reemission is characterized by low energy and momentum accommodation. Seidl and Steinheil (1974) derived a tangential momentum accommodation coefficient of 0.012 for helium scattered off of sapphire (Al_20_3), which was the most similar surface coating to an oxygen-covered surface. Gaposchkin (1994) infers the reflected scattering angle for helium from the data presented in the Seidl and Steinheil (1974) study and shows that θ_r increases as the incident angle θ_i increases. As the incident angle approaches 90°, θ_r is nearly equal to θ_i, which is consistent with specular reflection. Gaposchkin's work also suggests that the scattering distribution direction and lobe width depends on the incident velocity. For intermediate velocities (between 3 and 6 km/s), the scattering distribution is more diffuse. For lower velocities, scattering is more specular. Liu et al. (1979) found tangential momentum accommodation to be 0.046 for helium off of aluminum and anodized aluminum plates.

Laboratory molecular beam experiments with heavier gas constituents typically report higher energy and momentum accommodation. Minton et al. (2004) derived energy accommodation coefficients of ∼0.91 for CO_2 and Ar scattering at low incident angles. N_2 scattering experiments by N. A. Mehta et al. (2018) indicate that normal momentum accommodation is high (between 0.4 and 0.6), while tangential momentum accommodation is low (between 0 and 0.2). Murray et al. (2017) reports O and O_2 scattering with near-complete energy accommodation associated with thermal desorption off of an Au surface, while O and O_2 scattering off of SiO_2 and flat graphite surfaces appeared more specular with lower energy and momentum accommodation.

1.2 Gas-Surface Interactions in Orbit

Early efforts to constrain gas-surface interactions in space relied on experimental laboratory data. As space-based missions increased and on-orbit measurement techniques advanced, more studies were developed which used observational methods to determine the aerodynamic coefficients of different spacecraft from the attitude or orbital trajectory changes. In these studies, GSI and surface accommodation are typically investigated by considering the spacecraft attitude and geometry and comparing to different models. The on-orbit drag force is typically measured by either accelerometer data or observed orbital decay, where the product of density and C_D is determined from the observations. Paddlewheel satellite studies (K. Moe, 1966; Beletskii, 1970; Imbro et al., 1975) fall into this category, where paddlewheel satellites measure both spin and orbital decay. Spherical satellites (Bowman & Moe, 2005; K. Moe & Bowman, 2005; Pilinski et al., 2011) and satellites with complex geometries (Ching et al., 1977; Pardini et al., 2009; March et al., 2021) have also been used in these types of observational studies. Many of these studies have primarily assumed diffuse reflection with incomplete energy accommodation (DRIA) and have attempted to constrain the energy accommodation coefficient. In general, these studies have concluded that energy accommodation should be near-complete at altitudes near 200 km. At higher altitudes near 400-500 km, energy accommodation coefficients have been estimated to be closer to 0.85 (March, Visser, et al., 2019; March et al., 2021). A similar approach has been employed in Bernstein et al. (2020) through multi-satellite density comparisons, which is expanded upon in this paper. It is also important to recognize that results obtained from these types of observational methods can be dependent on modeled atmospheric densities and are thus subject to the model biases and uncertainties.

Much of the work towards understanding on-orbit GSI dynamics has focused on the role of atomic oxygen. Orbital measurements in the 1960s and 1970s from pressure

gauges and mass spectrometers led to the idea that satellite surfaces in orbit are contaminated with adsorbed molecules (Carter et al., 1969; Hedin et al., 1973). These early insights formed the foundation for the body of work of Moe and Moe (K. Moe et al., 1972; K. Moe & Moe, 1992; M. M. Moe et al., 1993, 1995; K. Moe & Moe, 2005), who modeled the adsorption of a monolayer of atomic oxygen using the Langmuir isotherm (K. Moe et al., 1972). Bowman and Moe (2005) and K. Moe and Bowman (2005) theorize that GSIs and the associated energy and momentum accommodation coefficients are dependent on atomic oxygen adsorption, which is expected to control the level of surface cleanliness. The result of these studies is that on-orbit reemission is considered to be primarily diffuse with high energy accommodation (>0.8) at altitudes studied (<300 km) due to surface contamination by adsorbed atomic oxygen. Additional support for this line of reasoning comes from a direct measurement of the reemission angle of scattered atomic oxygen from a vitreous carbon surface on the STS-8 Space Shuttle flight. Diffuse reemission with a nearly cosine distribution and near full accommodation was observed at an altitude near 225 km (Gregory & Peters, June 1986). Near-fully diffuse angular distributions of reemitted molecules were also measured near 180 km (Beletskii, 1970). At higher altitudes (800-1000 km), evidence of more quasi-specular reemission behavior has been observed for spacecraft materials (Harrison & Swinerd, 1996). To support these results, it has been proposed that surface contamination is lower at higher altitudes.

The separation of on-orbit force coefficients into drag and lift components signifies the dependence of the drag force on incident angle of the flow. Drag coefficients correspond to the force parallel to the flow, while lift coefficients correspond to the force perpendicular to the flow. Schamberg (1959) provides drag and lift coefficient expressions. Drag and lift coefficient expressions for a flat surface element as a function of incident angle are also derived by Schaaf and Chambre (1958). Ching et al. (1977) studied the ratio of lift to drag on the S3-1 satellite, which orbited at an altitude of 175 km. They found that the ratio of lift to drag force increases as energy accommodation decreases for all cases from specular to diffuse.

Recent missions highlight the ongoing interest in investigating GSI models and drag coefficients in orbit. The ΔDsat CubeSat mission (Virgili & Roberts, 2013) was designed to study how the drag coefficient changes for different satellite surface materials using steerable fins. This study only examines the drag forces for the surface area exposed to the flow, with no net lift forces, which allows the drag coefficient to be determined from the variation in the trajectory over time based on a free-parameter fitting scheme in the orbit determination process. The SOAR satellite (Crisp et al., 2021) was designed specifically to investigate how incident angle and surface material impact gas-surface interactions in orbit. Different panels will have different surface coatings to represent a range of expected GSI dynamics. For the SOAR experiment, data will only provide information for altitudes below 400 km. Thus, this is an area of emerging research and these inquiries currently do not have satisfactory answers.

DRIA is the standard model used to compute drag coefficients for satellites in orbit for research purposes. Studies which derive energy accommodation coefficients tend to suggest that, given diffuse reemission, energy accommodation decreases with increasing altitude and decreasing atomic oxygen (M. M. Moe et al., 1995; Pardini et al., 2009). However, this conclusion may still be limited by the fact that diffuse reemission is assumed. It is also possible that, as altitude increases and atomic oxygen decreases, reemission gets more quasi-specular with less tangential momentum exchange. This is something that the DRIA model framework is not able to test. Additionally, it is possible that different gas constituent species, like atomic oxygen and helium, scatter in different ways. DRIA with fixed α is not able to account for these scattering differences. Some DRIA implementations, like SESAM (Pilinski et al., 2013) and RSM (P. M. Mehta et al., 2014), try to partially incorporate this effect by implementing variable energy accommodation according to atomic oxygen number density, but these are still constrained by the assump-

tion of complete tangential momentum accommodation. Understanding the potential errors associated with the DRIA model is particularly significant when trying to calibrate atmospheric density models and datasets. The construction of thermospheric density and wind models from on-orbit observations depends on drag coefficients. Errors from C_D models, like DRIA, can lead to different biases at different altitudes/pressure levels.

Additionally, there is a disconnect in the theoretical foundations between the current state-of-the-art DRIA C_D models with their dependence on atomic oxygen adsorption and the laboratory experiment research on the effects of incident mass and angle. This motivates the present study into appropriate GSI modeling assumptions across a wide range of orbital conditions. Some work has been done to try to directly extrapolate laboratory experimental data to orbital drag coefficient models (Poovathingal et al., 2019; N. A. Mehta et al., 2018). The study presented in this paper does not directly fit laboratory data to an orbital drag coefficient model, but rather the authors consider insights from laboratory experimental results to constrain C_D model parameters which can then be applied to orbital density data processing and checked for consistency.

Following the body of theoretical and observational studies into GSI physics summarized in this section, the drag coefficient remains uncertain at upper thermospheric altitudes. This is a result of a lack of on-orbit measurements as well as variability in C_D model assumptions related to GSI dynamics and atmospheric constituents, which are further explored in Section 2. It is important to constrain this drag coefficient uncertainty because it can cause altitude-dependent density biases. In order to determine which C_D model assumptions may be most appropriate at upper thermospheric altitudes, the authors evaluate inter-satellite density consistency. The authors derive and compare densities for different shaped satellites, including GRACE (an elongated satellite) as well as a set of compact satellites, for a variety of different C_D models. This method is further described in Section 3. In Section 4, the authors present results highlighting which C_D models produce the most consistent densities across the atmospheric conditions sampled as well as further interpretation of the relevant C_D model assumptions. Concluding discussion is included in Section 5.

2 Current Drag Coefficient Model Formulations and Sensitivities

2.1 Incident Angle and Tangential Momentum Accommodation

When considering C_D sensitivity to GSI dynamics, incident angle of incoming molecules plays an important role that in many current models is not fully incorporated. Incidence angle describes the angle between the flow and the satellite surface normal. In this section, the influence of the incident angle is described. This helps to show why the drag coefficient for elongated satellites, compared to compact satellites, may be more sensitive to the nature of gas-surface interactions at high incidence angles.

Accommodation assumptions in drag coefficient models can explicitly impact the increase or decrease in drag. Making assertions about the effect on the drag requires careful specification of the orientation of the satellite surface relative to the incident flow, or the incident angle. The force on the satellite is given by the change in momentum along the velocity direction of the incident gas molecules. To help conceptualize the drag effects, the case of a flat plate moving perpendicular to the flow can be examined. Fig. 1 illustrates this scenario, showing both specular scattering (Fig. 1a) and diffuse scattering (Fig. 1b) cases for an incident molecule with velocity V_i impacting the plate and reemitting with velocity V_r. The incident molecule impacts the flat surface with an incidence angle of 0° from the surface normal. In the specular scattering case, energy E is conserved such that $E_i = E_r$ for the incident and reflected molecules. Then it follows that $|V_i| = |V_r|$. This means that in the flow direction normal to the satellite surface, the change in momentum which corresponds to the force on the satellite is maximized be-

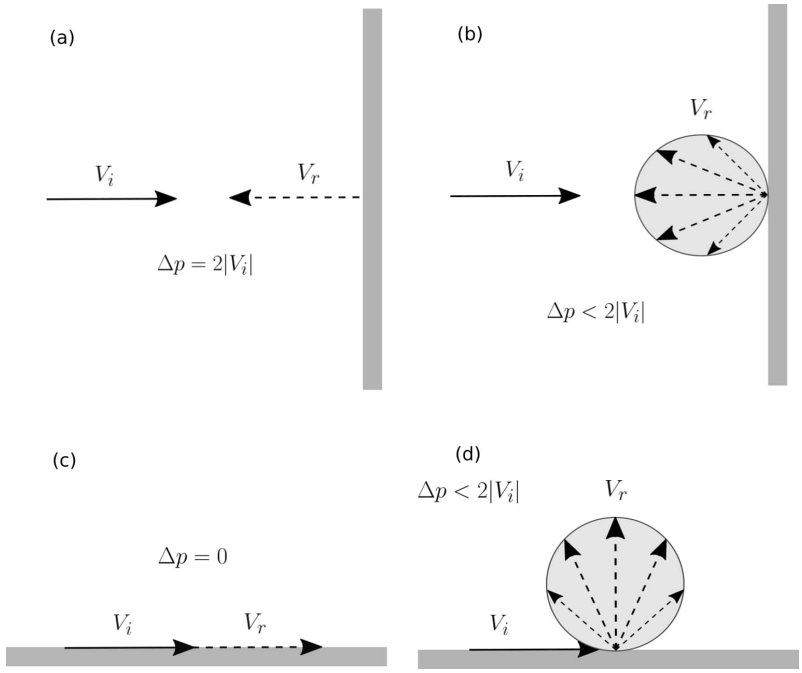

Figure 1. Specular scattering (a) and diffuse scattering (b) for a flat plate moving perpendicular to the flow direction V_i. Specular scattering (c) and diffuse scattering (d) for a flat plate moving parallel to the flow direction V_i.

cause V_r is equal in magnitude and opposite in direction to V_i. The change in momentum in this case becomes $2m_iV_i$. In the diffuse scattering case, the angular probability distribution of the reemitted molecule is a cosine distribution, meaning that the molecule has some probability of scattering in any direction. As such, integration over the probability distribution is required. The change in momentum between the reflected molecule and the incident molecule will be smaller than $2m_iV_i$ due to this cosine angular probability distribution of reflection. For the case of a flat plate moving perpendicular to the flow, diffuse scattering leads to smaller drag coefficients than those produced from specular scattering.

An additional scenario to consider is a molecule impacting a flat plate surface with an incident angle approaching 90°. This scenario can be visualized as a flat plate moving parallel to the flow, also shown in Fig. 1. In the completely specular scattering case shown in Fig. 1c, momentum and energy accommodation is 0. This means that the change in momentum is 0, and there is no drag from the incident molecule. In the diffuse scattering case shown in Fig. 1d, the cosine angular probability distribution of reflection suggests that the reemitted molecule will scatter in a random direction which will impart some amount of non-zero momentum transfer to the flat plate surface. For the case of a flat plate moving parallel to the flow, diffuse scattering leads to larger drag coefficients than those produced from specular scattering.

This example is helpful to show how an elongated satellite with extended surface area parallel to the flow is likely to be more sensitive to tangential momentum accommodation and the scattering direction than compact shaped satellites, especially as helium increases in the orbital environment. This is an important clarification to make as it highlights the significance of side scattering in C_D computations. As helium increases in the atmosphere, the thermal velocity increases due to helium's low molecular mass. This causes the ratio of the relative velocity between the satellite and flow to the ther-

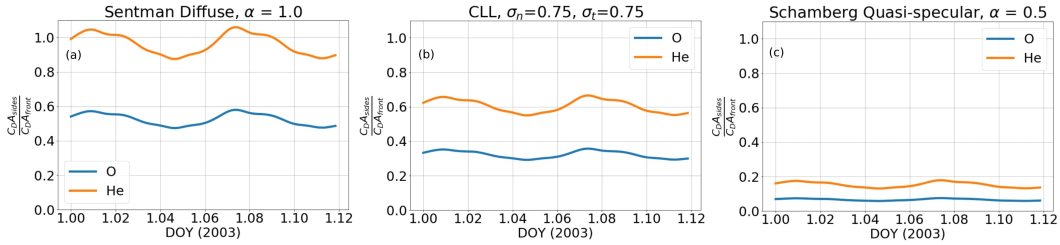

Figure 2. Force contributions of the side plates relative to the front plate for GRACE using the Sentman diffuse model (a), the CLL model (b), and the Schamberg model (c) in an atomic oxygen atmosphere (blue) and a helium atmosphere (orange).

mal velocity, known as the speed ratio, to decrease. Side scattering becomes increasingly important as the speed ratio decreases in helium-rich atmospheric conditions and random thermal motion increases the interactions of atmospheric gas with the surfaces parallel to the flow. As a result of increased impacts to the satellite, the drag coefficient increases by an amount dependent on the tangential momentum accommodation. Additionally, helium may have different gas-surface interaction dynamics with the satellite surface than other, heavier atmospheric constituents like atomic oxygen, which can impact the nature of the scattering. These concepts provide motivation for the study presented in this paper.

The effect of side scattering for an elongated satellite can be examined by comparing the relative force contributions of different panels on the Gravity Recovery and Climate Experiment (GRACE) satellite. The authors compute C_D for GRACE using the panel method, which is an analytical approach to geometry modeling that uses several flat plates to estimate a simplified satellite geometry and does not account for multiple scattering instances. An alternative approach to the panel method would be to use Direct Simulation Monte Carlo (DSMC) methods, which simulate rarefied gas flows to address shadowing and handle multiple scattering events. As the geometry of GRACE is relatively simple, the panel method should be appropriate for these conditions.

Fig. 2 shows the force contribution of the side panels relative to the front panel for GRACE for one day of the year in 2003 using three different C_D models. The force contribution for each panel is given by the product of the drag coefficient and the surface area A of the satellite panel. The ratio of the combined force contributions from the side panels to the front panel force contribution is shown for an atmosphere composed entirely of oxygen in blue and for an atmosphere composed entirely of helium in orange. Panel force contributions are computed using the Sentman diffuse C_D model in Fig. 2a, the CLL C_D model with 75% normal and tangential momentum accommodation in Fig. 2b, and the Schamberg quasi-specular C_D model with 50% energy accommodation in Fig. 2c.

For all three C_D models in Fig. 2, comparison of the blue and orange lines show that the side plates contribute approximately twice as much to the total force in a helium atmosphere than in an atomic oxygen atmosphere. This supports the notion that side scattering has a greater effect in helium-rich atmospheres. Additionally, comparison of the C_D models in Fig. 2 shows that as tangential momentum accommodation increases, the relative force contribution of the side plates increases. Tangential momentum accommodation is lowest in the quasi-specular Schamberg C_D model used in Fig. 2c, increases to 0.75 in the CLL C_D model in Fig. 2b, and maximizes to full accommodation in the Sentman diffuse C_D model in Fig. 2a. Tangential momentum accommodation significantly impacts the scattering angular distribution of a C_D model. As σ_t de-

creases, the scattering lobe becomes more specular. Side drag is reduced by decreasing σ_t. Drag coefficient sensitivity to GSI parameters are further explored in the following subsection.

2.2 Drag Coefficient Sensitivities for Different Shaped Satellites

Satellites of different shapes are sensitive in different ways to GSI parameters. This idea has already been introduced in the discussion of incident angle and lift effects in Section 2.1. To improve C_D modeling across LEO conditions, the GSI assumptions must be appropriate across satellite geometries. It is important to recognize how C_D for different geometries is expected to change according to various GSI assumptions and in different environmental conditions. Understanding these sensitivities will help with inferring C_D model limitations and inconsistencies from multi-satellite density comparisons, which is what the authors are undertaking with this study. For this reason, in this section C_D sensitivities to different modeling parameters are examined for both GRACE (an elongated satellite) and a compact sphere.

First, energy accommodation in the commonly-used DRIA C_D modeling framework can be examined. DRIA C_D modeling assumes diffuse reemission with $\alpha < 1$, where α is the single GSI input parameter. Many C_D modeling approaches which rely on DRIA assume a fixed value for α (Sutton et al., 2007; March, Visser, et al., 2019), while others allow α to vary according to certain atmospheric inputs (Pilinski et al., 2013). Because DRIA depends on only one GSI parameter, it is a simple and advantageous approach to physical C_D modeling. Fig. 3 shows Sentman DRIA C_D sensitivity to α for GRACE, represented by the blue lines, and a sphere, represented by the orange lines. In Fig. 3a C_D has been computed for an atmosphere composed entirely of atomic oxygen, while C_D in Fig. 3b has been computed for helium-dominated atmospheric conditions. Percentages included in Fig. 3 indicate C_D sensitivity to the range of α values from 0 to 1, computed as $\frac{\max(C_D)-\min(C_D)}{0.5*(\max(C_D)+\min(C_D))}*100$. The drag coefficient decreases for both GRACE and the sphere as α increases, since increasing energy accommodation results in smaller reflected velocities. Drag coefficient sensitivity percentages are similar for both GRACE and the sphere. Comparison of C_D in atomic oxygen-dominated conditions in Fig. 3a and helium-dominated conditions in Fig. 3b reveals that C_D for the sphere remains nearly unchanged as the atmospheric composition decreases in mass. In contrast, C_D for GRACE increases significantly in the helium-dominated atmosphere compared to the oxygen-dominated atmosphere due to side scattering effects discussed in Section 2.1. Thus, GRACE is more sensitive to incident mass effects than the sphere for the Sentman DRIA C_D model.

In contrast to DRIA, the CLL C_D model has two input GSI parameters: the normal and tangential momentum accommodation coefficients. CLL C_D modeling allows reemission to be diffuse ($\sigma_n = \sigma_t = 1$), specular ($\sigma_n = \sigma_t = 0$), or quasi-specular ($0 < \sigma_n < 1$ and $0 < \sigma_t < 1$). CLL can also be parameterized for back-scattering by setting $1 < \sigma_t < 2$ (Lord, 1991), however this approach is not considered to be relevant in the context of physical on-orbit GSIs and thus does not apply to the work in this paper. Fig. 4 shows CLL C_D sensitivity to σ_t, where σ_n has been fixed to 0.5, for GRACE and a sphere represented by blue and orange lines, respectively. Just like in Fig. 3, Fig. 4a represents atomic oxygen atmospheric conditions and Fig. 4b represents helium atmospheric conditions. Percentages in Fig. 4 are computed the same way as in Fig. 3. As σ_t increases, C_D increases for both GRACE and the sphere. As σ_t approaches 1, the reemission angle gets closer to the surface normal, causing drag to increase for high-incident angle impacts. Drag coefficient sensitivity to σ_t for the sphere remains nearly unchanged between the atomic oxygen and helium conditions. GRACE C_D sensitivity to σ_t, however, significantly increases in the helium-dominated atmospheric conditions. In other words, GRACE C_D changes more in response to changing σ_t in helium-rich conditions

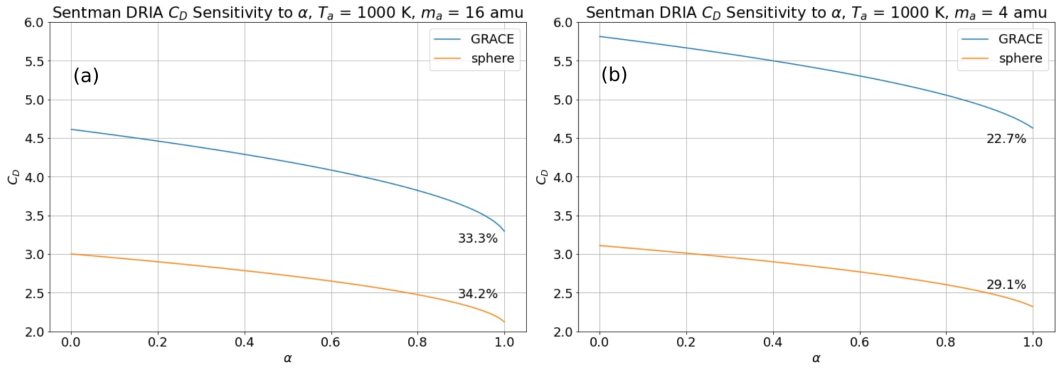

Figure 3. Sentman DRIA C_D sensitivity to the energy accommodation coefficient parameter for GRACE (blue curve) and a sphere (orange curve) in 100% atomic oxygen conditions (a) and 100% helium conditions (b).

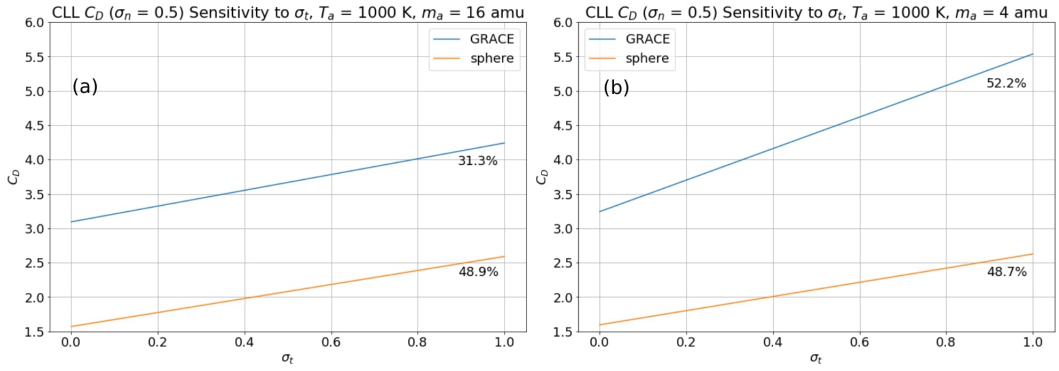

Figure 4. CLL C_D sensitivity to the tangential momentum accommodation parameter σ_t for GRACE (blue curve) and a sphere (orange curve) in 100% atomic oxygen conditions (a) and 100% helium conditions (b). Fixed $\sigma_n = 0.5$.

than in atomic oxygen-rich conditions. Just like for the DRIA model, the CLL C_D model for GRACE is more sensitive to incident mass effects than for the sphere.

Fig. 5 shows CLL C_D sensitivity to both σ_n on the x-axis and σ_t on the y-axis for GRACE in atomic oxygen conditions (Fig. 5a), GRACE in helium conditions (Fig. 5b), a sphere in atomic oxygen conditions (Fig. 5c), and a sphere in helium conditions (Fig. 5d). The drag coefficient is highly sensitive to both σ_n and σ_t. GRACE C_D in helium-rich conditions, shown in Fig. 5b, exhibits the greatest variability of the four panels. Additionally, C_D for GRACE changes more significantly than for a sphere as conditions transition from an atomic oxygen atmosphere to a helium atmosphere.

Figures 3, 4, and 5 show that both the elongated satellite (GRACE) and the sphere are more sensitive to tangential momentum accommodation than energy accommodation, especially in helium-rich conditions. This discussion motivates using satellites with different shapes for evaluating C_D model assumptions. This research approach follows in the steps of previous investigations of lift-to-drag measurements. The behavior of low-incidence angle interactions compared to high-incidence angle interactions leads to differences in the C_D response to gas-surface interaction parameters. For this research, C_D model assumptions are evaluated in order to constrain appropriate on-orbit gas-surface interaction parameters.

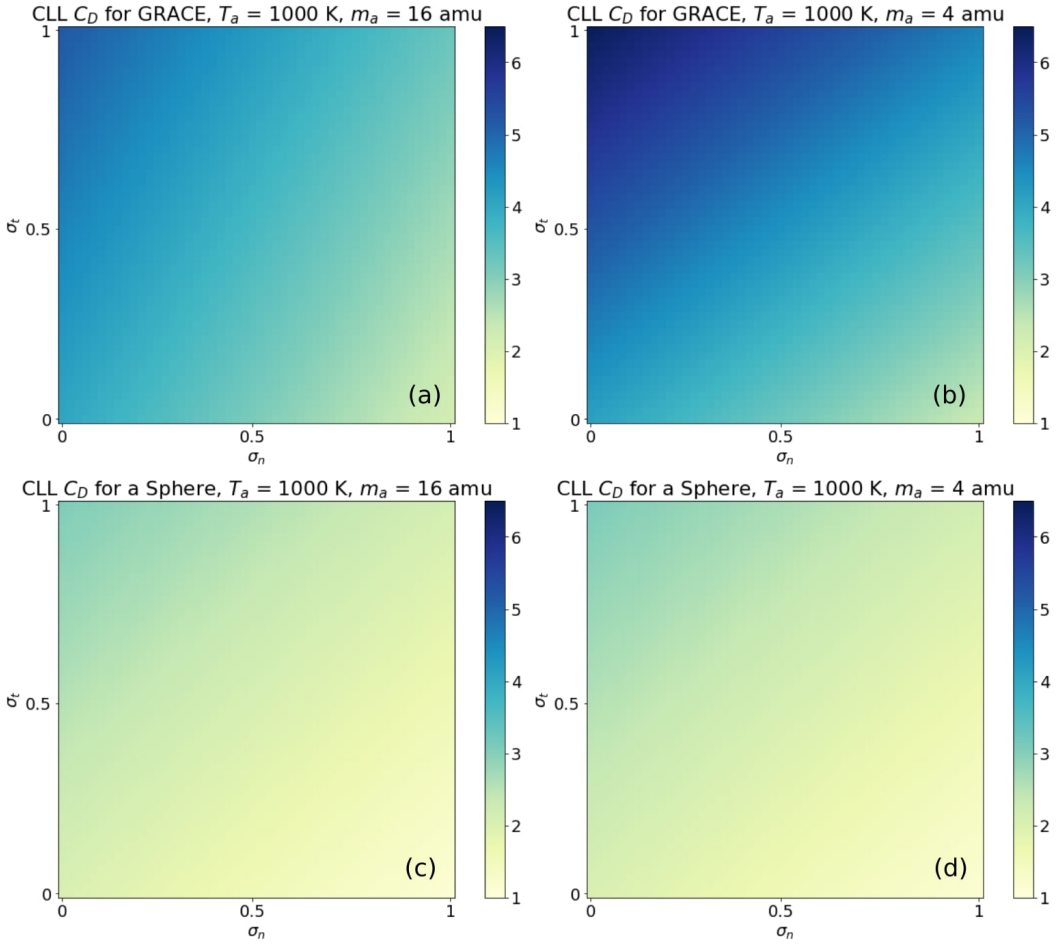

Figure 5. CLL C_D sensitivity to normal and tangential momentum accommodation for GRACE in atomic oxygen conditions (a), GRACE in helium conditions (b), a sphere in atomic oxygen conditions (c), and a sphere in helium conditions (d).

3 Method

The analysis presented in this paper involves evaluating inter-satellite density consistency in order to constrain and improve physical gas-surface interaction assumptions in C_D models, especially in helium-rich regimes. The density comparisons are made between GRACE (an elongated satellite) and a set of compact, or near-spherical, satellites in order to evaluate the incidence angle effect. This analysis method extends the approach in Bernstein et al. (2020), in which density discrepancies between GRACE and a selection of compact satellites were analyzed over four distinct week-long time periods. Density discrepancies are defined by Eq. (4):

$$\Delta R = \left(\frac{\rho_{obs}}{\rho_{mod}}\right)_{GRACE} - \left(\frac{\rho_{obs}}{\rho_{mod}}\right)_{sphere} \tag{4}$$

The density values in Eq. (4) represent weighted averages along the orbit, referred to as effective densities. The density discrepancy metric ΔR in Eq. (4) is also approximately equal to a function of C_D ratios (see Section III in Bernstein et al. (2020)). Examining observed-to-modeled density ratios allows for the comparison of analogous observed quantities for GRACE and the compact satellites while removing differences in densities due to the satellites not sampling identical altitudes. This is based on the assumption that atmospheric model bias should be the same for GRACE and the compact satellites in the comparisons. To better account for altitude-dependent model biases, a fitting scheme is implemented which is discussed more in Section 3.2.

Effective densities for the compact satellites are obtained from orbital Two-Line Element (TLE) data following the procedure in Picone et al. (2005). The United States Space Command (USSPACECOM) 18th Space Control Squadron (18SPCS) archives orbital tracking data for most known Earth-orbiting artificial satellites in the form of TLE entries, which provide an expansive record of historical orbital element information. Effective densities are computed from TLEs based on how the satellite orbit changes over time, represented by the change in mean mean motion. Effective densities for GRACE come from accelerometer-derived density datasets from Sutton et al. (2007). These densities are scaled with force coefficients modeled using a variety of C_D modeling frameworks and integrated along time intervals consistent with the TLE-derived effective densities.

The time periods of analysis in Bernstein et al. (2020) were selected to sample a variety of solar and geomagnetic conditions while benefiting from the fidelity of the Thermosphere Ionosphere Electrodynamics General Circulation Model (TIE-GCM) (Qian et al., 2014). The results indicated that tangential momentum accommodation plays a significant role in deriving consistent densities from drag data. However, various limitations were introduced into the analysis as a result of these time periods and data/model considerations. These include the signal-to-noise ratio associated with the TLE data, TLE and accelerometer dataset differences (Bernstein et al., 2021), local time and latitude differences between the orbits of GRACE and the compact objects, sensitivity to atmospheric model error, and challenges associated with making statistically significant conclusions given the small amount of data. This work expands upon the study in Bernstein et al. (2020) by addressing each of the above-mentioned limitations and proposing improvements to gas-surface interaction modeling based on density consistency results.

First, it was important to expand the datasets temporally. Among other advantages, this enables the authors to have enough data to find satellite orbit conjunctions for more reliable density comparisons. It also is helpful for increasing some of the TLE signal-to-noise through averaging, which enables the use of solar minimum TLE data for which atmospheric helium is in greater abundance.

Refining the density discrepancy analysis from Bernstein et al. (2020) to be robust against uncertainty can be summarized with four distinct measures: 1) significant data

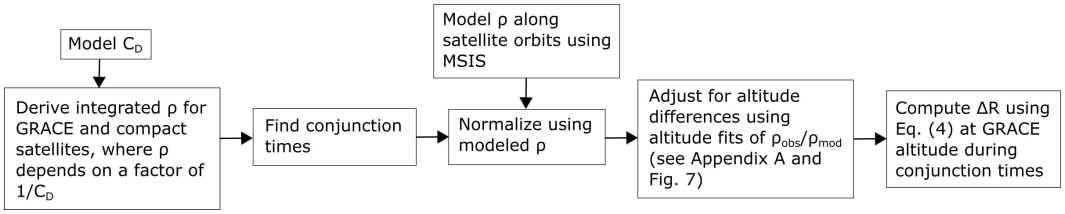

Figure 6. Flow chart summarizing how GRACE and compact satellite data is processed to obtain the density discrepancy metric, ΔR

expansion, 2) increasing the time window of effective density integration to 8 days, 3) making comparisons at narrower local time and latitude conjunctions, and 4) fitting the vertical structure of observed-to-modeled density ratios to the ratio of two Bates profiles in order to compare data from compact satellites at a range of altitudes. These are concerted efforts to address possible sources of error in ΔR that are not C_D-related in order to more convincingly make conclusions about C_D model effects. Each of these measures will be described in the following subsections. A flow diagram summarizing how ΔR is obtained from GRACE and compact satellite data is included in Fig. 6, the details of which are further described in the following subsections.

3.1 Extending and Refining Aerodynamic Drag Observations during Conjunctions

To expand the datasets, this analysis covers the full range of available GRACE accelerometer-derived density data (Sutton et al., 2007; P. M. Mehta et al., 2017) from 2002-2010, inclusive. This is a significant increase in time covered, as in Bernstein et al. (2020), only four weeks of data were used. The empirical Naval Research Laboratory's Mass Spectrometer and Incoherent Scatter Extended (MSIS) (Picone et al., 2002) atmospheric model has been used to obtain composition and neutral density for this time period. This expanded time period covers the deep solar minimum years from 2008-2010 and thus samples atmospheric conditions with more helium.

TLE data has decreased signal-to-noise during deep solar minimum times. This can be addressed using insights from the TLE variability and error analysis described in Bernstein et al. (2021). The time window of integration in the TLE mean mean motion processing is selected to be a moving window of 8 days. This means that the effective densities derived from TLE data for the compact satellites are densities that have been averaged over 8 days. A multi-day time window was chosen since relative error between TLE-derived and accelerometer-derived densities decreases as the integration time interval increases (Bernstein et al., 2021). However, integrating between 8 and 20 days produced very similar relative error profiles across density bins. Choosing the smallest time interval in this range is preferable in order to avoid over-averaging. Choosing to integrate over 8 days is also advantageous for avoiding certain short-term, solar-related periodicities, like the 13.5 day period associated with active solar longitudes and the tilted dipole structure which is observed in the solar wind and interplanetary magnetic field (Nayar, 2006; Bouwer, 1992). It is relevant to note here that Emmert (2009) used 3-6 days as the time integral when processing TLEs to derive long-term density trends in the thermosphere.

The GRACE accelerometer densities have been averaged over the same 8-day moving windows to ensure reliable comparisons with the compact satellites' TLE data. Consequently, many local or short-term density signatures have been averaged over in favor of increasing the signal-to-noise in the TLE densities. This highlights the trade-off between resolution and noise as a result of using TLE data. In addition to increasing the

Table 2. High-Inclination Compact Satellites

NORAD ID	Common Name	Perigee h (km)	i (deg)	e	A/m estimate (m^2/kg)
00045	TRANSIT 2A	600	66.7	0.025	0.00673
00046	SOLRAD 1	590	66.7	0.023	0.0107
00060	EXPLORER 8	370	49.9	0.035	0.011
00932	EXPLORER 25	530	81.4	0.115	0.0091
02826	SURCAL NRL 160/CALSPHERE 3	725	69.9	0.0005	0.0815
02909	SURCAL NRL 150B/CALSPHERE 4	685	69.9	0.0003	0.0834
06073	VENUS LANDER	200	52.0	0.127	0.00181
07337	COSMOS 660	390	83.0	0.054	0.00534
12138	COSMOS 1238	415	83.0	0.080	0.00531
14483	COSMOS 1508	395	83.0	0.082	0.00537
20774	COSMOS 2098	405	83.0	0.090	0.00546
23278	COSMOS 2292	400	83.0	0.095	0.00531

time window of integration, only leading GRACE satellite density data has been used in these comparisons. This is due to the identification of the density bias associated with trailing GRACE satellite data in Bernstein et al. (2021). GRACE A is the leading satellite from 2002 to late 2005, and GRACE B is the leading satellite from late 2005 onward.

Additional measures to make the GRACE and compact satellite density comparisons robust include finding conjunction times for the satellite orbits in the comparison. This involves selecting comparison times where the local time and latitude of the two satellite orbits match within a reasonable range, thereby further ensuring that they should be sampling similar orbital and density conditions. This means constraining the available compact satellites to only those objects with high inclinations ($>\sim 50°$) because GRACE inclination is approximately 87°. Table 2 lists these high-inclination compact satellites. For the density comparisons between GRACE and the compact satellites, both local time and latitude conjunctions are found. Local time matching is done by comparing the local time at perigee for the compact object with the local time of the ascending or descending node for GRACE near the middle of the 8-day window. For windows in which these local times match within ±1 hour, latitude filtering is employed for the GRACE data within the window. GRACE data in the window for which GRACE latitude is within ±20° of the latitude at perigee for the compact satellite is used to compute the GRACE effective densities for those conjunction windows. Finding conjunctions in local time and latitude between GRACE and the compact objects helps to justify that the satellites should be sampling similar observed and modeled atmospheric density conditions in the same 8-day window.

3.2 Density Comparisons at GRACE Altitude Through Bates Profile Fitting

It is clear from Table 2 that the set of compact satellites has a wide range of perigee altitudes spanning ∼200 - 700 km. GRACE, in contrast, orbits at altitudes between ∼475-525 km in the analysis time period prior to 2010. These significant altitude differences between GRACE and some of the compact satellites can lead to differences in derived densities as well as measured-to-modeled density ratios. These altitude-dependent differences might interfere with the inconsistencies that can be attributed to C_D model error. For this reason, the authors needed to find a way to mitigate the altitude differences among the objects. Simply removing all of the compact objects with perigees that extended beyond a reasonable threshold, like ±50 km from GRACE, was not a desirable option because this would significantly cut the amount of usable data in the analysis.

Instead, a fitting scheme was implemented to fit the altitude structure of measured-to-modeled density ratios for the compact satellites to the ratio of two Bates profiles (Bates,

Table 3. Sentman Diffuse Density Ratio Altitude Fit Parameters

GRACE Avg. He/O	C_1	C_2	C_3	RMSE
0.04	0.7153	1.140	1015.2	0.0779
0.1	0.6902	1.1774	942.9	0.0595
0.23	0.6168	1.1804	793.7	0.0597

1959). This fitting scheme is presented in detail in Appendix A and is based on the assumption that exospheric temperature differences are primarily causing the offset between the observed and modeled densities. The purpose of obtaining a physically-informed vertical profile of measured-to-modeled density ratio for the compact satellites was to be able to attain a value for $\frac{\rho_{obs}}{\rho_{mod}}$ for a spherical satellite at the precise location of GRACE. This value comes from the fitted density ratio profile, which is constructed using data from each of the compact satellites.

Following the procedure in Appendix A, a parametric system of equations for the ratio of two mass density profiles was obtained (see Eq. (A6)). A simplified version of this expression is shown in Eq. (5), where an 'observed' density profile is signified by the superscript A and a 'modeled' density profile is signified by the superscript B.

$$\frac{\rho^A}{\rho^B} = f(C_1, C_2, C_3)$$
$$\begin{cases} C_1 = \frac{n^A_{O,\ell}}{n^B_{O,\ell}} \\ C_2 = \frac{n^A_{He,\ell}}{n^B_{He,\ell}} \\ C_3 = T^A_\infty \end{cases} \tag{5}$$

In Eq. (5), T_∞ represents exospheric temperature, and the subscript ℓ indicates the lower boundary altitude of the diffusive equilibrium region. Eq. (5) has been derived from Bates number density profiles and leverages model output from MSIS in order to reduce the number of unknown parameters. The three parameters to fit are represented by C_1, C_2, and C_3. To maintain a reasonable number of parameters to fit, the thermosphere is assumed to be composed only of O and He at the satellite altitudes of interest.

Non-linear least squares fitting of Eq. (5) to the $\frac{\rho_{obs}}{\rho_{mod}}$ data for the compact satellites is performed. Note that GRACE data is not used for this fitting process, since the goal of the fitting scheme is to get an altitude profile of measured-to-modeled density ratios for the compact satellites from which a fitted value for the compact satellites at GRACE's location can be obtained. The density ratio fits include C_D effects, since the observed density data used to construct the fit depends on the C_D model used. Thus, altitude profiles were fit to the density ratios for each C_D model used in the analysis. Additionally, the data used to construct the fit profiles were averaged into three bins. The bins were sorted by average atmospheric helium-to-oxygen mass ratio along the GRACE orbit. Helium-to-oxygen mass ratio is computed using MSIS. Fitted altitude profiles of observed-to-modeled density ratios for the compact satellites are shown for the three average He/O bins for two C_D model cases in Fig. 7. Fits for the compact satellite observed-to-modeled density ratios are shown for the Sentman diffuse C_D model in Figs. 7a, 7b, and 7c as well as for the Schamberg specular model in Figs. 7d, 7e, and 7f. Tables 3 and 4 include fit parameter estimates and root mean squared error (RMSE) for the selected Sentman diffuse and Schamberg specular C_D model cases.

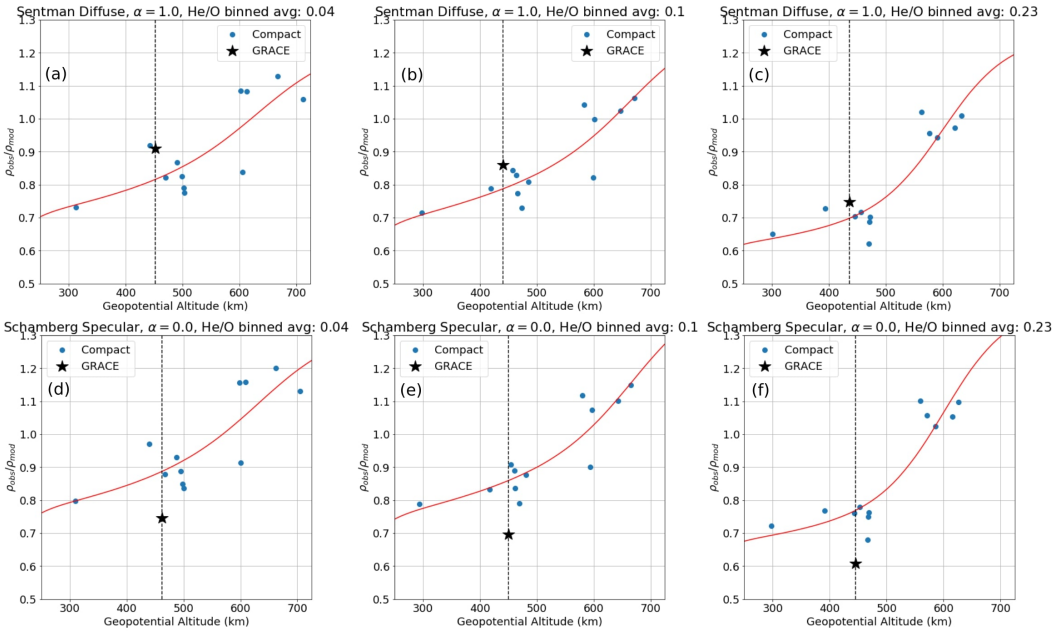

Figure 7. Altitude fits of the observed-to-modeled density ratio for the compact satellites are shown by the red curves. Observed densities from panels (a), (b), and (c) have been derived using the Sentman diffuse C_D model. Observed densities from panels (d), (e), and (f) have been derived using the Schamberg specular C_D model. Compact satellite observed-to-modeled density ratios are marked by the round blue markers. The average GRACE density ratio is marked by the black star, and the interpolated geopotential altitude location of GRACE is marked by the dashed black vertical line.

Table 4. Schamberg Specular Density Ratio Altitude Fit Parameters

GRACE Avg. He/O	C_1	C_2	C_3	RMSE
0.04	0.7740	1.232	1013.9	0.0773
0.1	0.7553	1.330	939.6	0.0596
0.23	0.6732	1.317	793.2	0.0636

In Fig. 7, the panels show the data and fits for the three distinct He/O bins, where the average He/O mass fraction increases in the atmosphere from the left-most panel to the right-most panel. These He/O ratios are averages that have been weighted by drag along the time intervals of integration (8 day periods) for the effective density, which covers many orbits of the satellite. In other words, these He/O ratios are multi-day weighted averages along the orbit of GRACE. Compact satellite observed-to-modeled density ratios are marked by the round blue markers. The density ratio altitude profile fits based on the ratio of two Bates profiles are included as the red curves. The interpolated geopotential altitude location of GRACE is marked by the dashed black vertical line. The average GRACE observed-to-modeled density ratio is included as the black star. Note that this value is computed as the average GRACE effective density corresponding to conjunctions with each individual compact satellite, described in Section 3.1.

Note that the vertical structure of the density ratio is influenced by the C_D model. The values of the fitted density ratio profile for the compact satellites are higher for the specular C_D model case than for the diffuse C_D model case. This suggests that, for the compact satellites, the observed densities derived with specularly modeled C_D are larger than the observed densities derived with diffusely modeled C_D. This is because specular C_D is smaller than diffuse C_D for spherical satellites, and the derived densities are scaled by $\frac{1}{C_D}$. Fig. 7 also helps to visualize how GRACE density ratios compare to the compact satellite density ratio fits. In the diffuse C_D model case, the average GRACE observed-to-modeled density ratio, represented by the black star, is too high compared to the red compact satellite density ratio fit line, especially in the left-most panel (Fig. 7a) which shows data for the smallest He/O bin. This suggests that GRACE densities are too large compared to the compact satellite densities in these He/O conditions due to C_D mismodeling by the Sentman diffuse model at these altitudes. Looking at the specular C_D-based density ratios in Figs. 7d, 7e, and 7f, GRACE average density ratios are more significantly offset from the compact satellite density ratio fit line for all three He/O bins. This is consistent with the finding that specular C_D for GRACE is likely too high compared to diffuse C_D, so specular C_D modeling yields densities for GRACE that are too low. This is an important finding, as it shows that modeling the drag coefficient with specular scattering yields significant density inconsistencies between the GRACE and compact satellites. Specular scattering drives the C_D up for GRACE due to the front-plate scattering dominating the drag force. Specular scattering on the front plate yields the maximum momentum exchange (more than diffuse) in GRACE gas-surface interactions, as is illustrated in Section 2.1.

For both the diffuse and specular C_D cases, and for all three He/O bins, the fits suggest that the MSIS model overpredicts the atomic oxygen number density and underpredicts the helium number density. This is shown in Tables 3 and 4, where C_1, the estimated observed-to-modeled atomic oxygen number density ratio at the lower boundary, is less than 1 for all cases. The estimated fit parameter C_2, the observed-to-modeled helium number density ratio at the lower boundary, is greater than 1 for all cases.

To compute ΔR, the value of the fit profile at GRACE's altitude (where the fit line intersects with the vertical black dashed line in Fig. 7) is subtracted from the average observed-to-modeled density ratio for GRACE at conjunctions. Recall that the purpose of doing the fitting was to resolve differences in perigee altitudes of the compact satellites while still making use of all of the compact satellite density data. This procedure to compute ΔR is implemented for a variety of C_D model cases and for each of the three GRACE He/O mass fraction bins.

4 Results

Density discrepancies between GRACE and high-inclination compact satellites for the years 2002-2010 are shown in Fig. 8. The ΔR values are sorted and binned accord-

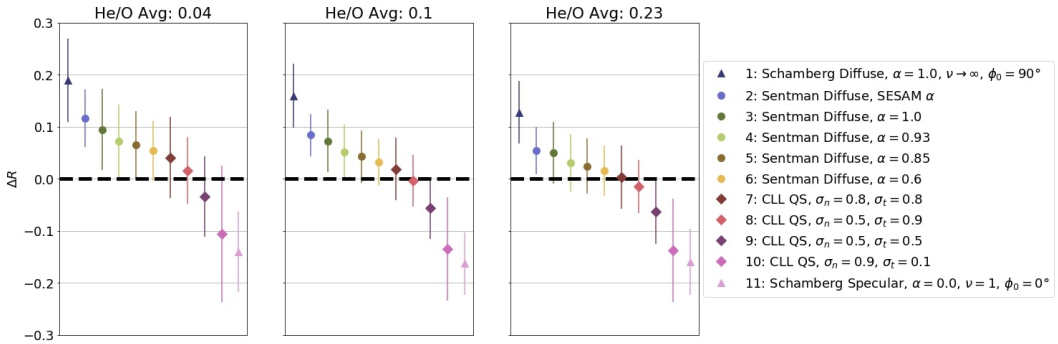

Figure 8. Binned average density discrepancies between the leading GRACE satellite and compact satellites. Each panel include ΔR results for one of the three He/O bins labeled by the panel title. Different colors represent different C_D models, and different markers are used to show that some C_D models share similar GSI assumptions. Vertical error bars represent the RMSE associated with the density ratio altitude profile fits.

ing to the He/O mass fraction along the GRACE satellite orbit. Each panel in Fig. 8 shows the ΔR results for one of the three He/O bins indicated by the panel title. The left-most panel includes density discrepancy data in low-helium atmospheric conditions, while the right-most panel includes data in helium-rich atmospheric conditions. Different colors represent different C_D models used to derive the effective density ratios. Each of the colored data points are separated by a small amount in the horizontal direction in order to distinguish C_D model differences. Vertical error bars represent the root mean squared error of the compact satellite density ratios compared to the best-fit density ratio altitude profile.

The C_D models used are numbered and labeled in the legend of Fig. 8. The C_D model labels in general include a combination of model name (Sentman, Schamberg, or CLL), reemission characteristics (diffuse, quasi-specular (QS), or specular), and accommodation coefficient parameters (α, σ_n, and σ_t). For model #2: Sentman Diffuse with SESAM α, a fixed value for energy accommodation is not included because α varies based on atomic oxygen pressure for this model (Pilinski et al., 2013). Different marker shapes are used to help differentiate the model names: triangles for Schamberg models, circles for Sentman models, and diamonds for CLL models.

A horizontal black dashed line is included at $\Delta R = 0$ in each of the panels of Fig. 8. Proximity to this zero-line is one indicator that the inter-satellite density comparisons are consistent for a given C_D model. As ΔR shifts away from 0, the orbital evidence may be indicating that the corresponding C_D model is not appropriate in the atmospheric conditions examined.

A few key trends can be discerned from the ΔR results in Fig. 8. Recall that scattering in gas-surface interactions can generally be described as diffuse, specular, or quasi-specular based on reemitted velocity. Diffuse and specular scenarios cover opposite ends of the range of possible scattering dynamics, while the quasi-specular descriptor is more broad and can be used to describe scattering that falls in between the diffuse and specular cases, characteristic of incomplete momentum accommodation. In Fig. 8, all of the C_D models which implement diffuse scattering (models #1-6) produce average ΔR values that are greater than zero across the atmospheric conditions examined. The completely specular C_D model (model #11) yields ΔR values that are less than zero in all three He/O bins. The quasi-specular C_D models (models #7-10) produce ΔR values that

fall between those associated with the diffuse and specular models, where ΔR decreases as the QS models get increasingly closer to specular.

To interpret these trends, it is helpful to return to the discussion in Section 2.1 on the effects of tangential momentum accommodation and incident angle for elongated satellites. The inter-satellite density comparisons, as well as the relative force contributions of the side panels to the front panel for GRACE shown in Fig. 2, indicate that the scattering on the front plate dominates the drag force on GRACE. As the amount of helium increases in the atmosphere, the effect of the assumed side panel GSI dynamics on the total drag force is greater. Since $\Delta R > 0$ for the diffuse C_D models (models #1-6) in Fig. 8, the inter-satellite density comparisons are indicating that the observed-to-modeled density ratio for GRACE is too high compared to the sphere density ratio. Given that the observed densities are inversely proportional to the drag coefficient, this indicates that diffuse C_D is too small for GRACE with respect to the C_D response for the sphere. Diffuse reemission would produce less drag than specular reemission on the front panel of GRACE due to the low incident angle of the GSIs (see Fig. 1), which explains why diffuse C_D may be too low for GRACE at these atmospheric conditions resulting in positive density discrepancies between GRACE and the spheres. It is worth noting here that models #1 (Schamberg diffuse) and #3 (Sentman diffuse) yield significantly different ΔR values even though they both assume diffuse scattering with complete accommodation. This may be because Sentman and Schamberg implement different formulations of diffuse scattering, which causes the two models to give different C_D values for a sphere and even more so for an elongated satellite like GRACE. For one thing, Sentman (1961) and Schamberg (1959) use different expressions for most probable velocity. Additionally, diffuse scattering in Sentman's model is represented with a cosine angular distribution, while Schamberg's diffuse scattering distribution is modeled with a cone shape (Sentman, 1961; Schamberg, 1959). As such, these two diffuse GSI models do not produce identical C_D values, especially for elongated shapes, leading to significant differences in ΔR associated with each model.

In contrast, Fig. 8 shows that ΔR is too low when a specular C_D model (model #11) is used. This is because the density ratio for GRACE is too low in this case, as was shown in Fig. 7. This indicates that the specular C_D for the elongated GRACE satellite is too high across the range of atmospheric He/O conditions presented here. As discussed in Sections 2.1 and 3.2, specular scattering increases the C_D for GRACE because the large change in momentum associated with specular scattering on the front plate dominates the drag force on GRACE. A similar argument can be made to discredit model #10, a CLL QS model with $\sigma_n = 0.9$ and $\sigma_t = 0.1$ which yields scattering that is close to specular, based on the significantly negative ΔR results associated with this C_D model.

The observed inter-satellite density comparisons in Fig. 8 also clearly show the effect of decreasing energy accommodation in diffuse C_D models on density consistency. As α decreases in the fixed DRIA models (models #3-6), average ΔR in all three He/O bins decreases and gets closer to zero. This follows the discussion on C_D sensitivity to model parameters in Section 2.2, where it was shown in Fig. 3 that diffuse C_D gets larger as α decreases. Since GRACE C_D increases as α decreases, the observed-to-modeled density ratios for GRACE get smaller as C_D DRIA models with less energy accommodation are used. This results in smaller ΔR values associated with diffuse C_D models which assume less energy accommodation.

In comparing the three panels of Fig. 8 from left to right, it is clear that the ΔR values associated with each C_D model shift down as helium increases in the atmosphere. The magnitude of this shift depends on C_D model assumptions. This trend shows how helium drives the speed ratio. As helium increases in the atmosphere, the speed ratio decreases causing C_D for the elongated GRACE satellite to increase. As the GRACE C_D increases with more helium, GRACE derived densities decrease resulting in a measurable decrease in ΔR. This is the case for all C_D models shown in Fig. 8, however the

diffuse C_D models yield the greatest decrease in ΔR from the left bin to the right bin. This also is aligned with the discussion in Section 2.1, since more helium in the atmosphere leading to increased diffuse scattering at high incidence angles, like on the side panels of GRACE, causes C_D to increase more than if the side scattering were specular in nature. Thus, the behavior of the observed ΔR as helium increases in the atmosphere follows the theoretical examination of increased drag at high incidence angles from GSI models that assume full tangential momentum accommodation.

Examination of models #7-10 in Fig. 8 reveals that a quasi-specular C_D model with incomplete normal and tangential momentum accommodation is more appropriate than a diffuse or specular model at the altitudes and atmospheric conditions sampled in this analysis. Since some of the QS models produce ΔR values that fall above the $\Delta R = 0$ line and other QS models produce ΔR values below the $\Delta R = 0$ line, it follows that there should be an optimal set of GSI accommodation parameters which yield $\Delta R = 0$. Based on ΔR proximity to zero in all three bins in Fig. 8, model #8: CLL QS with $\sigma_n = 0.5$ and $\sigma_t = 0.9$ appears to be a reasonable candidate for an appropriate GSI model at these altitudes and He/O conditions. It is also possible that helium may scatter differently than atomic oxygen when interacting with a satellite surface, which could mean that the optimal GSI assumptions in a helium-rich atmosphere might not be the same as the optimal GSI assumptions in an atomic-oxygen rich atmosphere. Further analysis which samples altitudes with a greater helium concentration is needed to confirm this, though this idea is supported by the result that there is a C_D model that appears to work best in only one of the He/O bins in Fig. 8. Model #7, CLL QS with $\sigma_n = 0.8$ and $\sigma_t = 0.8$, appears to produce consistent inter-satellite density comparisons in the highest average He/O conditions in the right panel of Fig. 8. However in the left panel of Fig. 8 representing the lowest average He/O conditions, model #7 appears to be inappropriate based on its corresponding ΔR value that is greater than zero. This may suggest that the optimal C_D model assumptions may shift as helium increases in the atmosphere.

To better visualize the angular distributions of the diffuse and QS models used in this study, the CLL scattering kernels which correspond to the GSI parameters in models #3 and #7-9 can be examined. It is worth noting that model #3, Sentman diffuse with complete energy accommodation, can be replicated with a CLL model assuming $\sigma_n = 1$ and $\sigma_t = 1$. Scattering kernels for the CLL models are given through probability distribution functions for normal and tangential velocity components. Scattering angular probability distributions for a set of accommodation parameters can be obtained through Direct Simulation Monte Carlo (DSMC) simulations (Lord, 1991; Turansky, 2012). It should be noted that the DSMC implementation of the CLL model depends on two input parameters: α_n and σ_t (Lord, 1991). In contrast, the analytical CLL C_D expressions depend on a different set of accommodation parameters: σ_n and σ_t. In order to represent the assumed GSI of CLL C_D models with DSMC scattering kernels, the authors make use of a fitted relationship between σ_n and α_n derived by Walker et al. (2014):

$$\sigma_n = 1 - \sqrt{1 - \alpha_n} \tag{6}$$

Eq. (6) was derived through iterative validation and Latin hypercube sampling with C_D values computed by NASA's DSMC Analysis Code. Eq. (6) is not the full fitted relationship between σ_n and α_n derived by Walker et al. (2014) (which includes two equations), however, Eq. (6) is all that is needed for the purposes of this study since for a given value of σ_n, there is only one possible solution for α_n between 0 and 1.

Fig. 9 includes DSMC CLL scattering angular probability distributions generated from 500,000 sample particles. The incident particles are monoenergetic beams of atomic oxygen with a fixed incident velocity of 7.5 km/s at a specified incident angle from the surface normal. Figs. 9a and 9b show the DSMC-generated reemission angular probability distributions assuming CLL GSI with $\sigma_n = \alpha_n = 1.0$ and $\sigma_t = 1.0$ at an incident

angle of 0° and an incident angle of 85°, respectively. At both low and high incident angles, these model assumptions exhibit diffusive scattering with a cosine distribution. As a reminder, these diffusive scattering assumptions are adopted by all C_D models with the description 'diffuse' in their label (models #1-6).

In contrast, the changes associated with decreasing normal and tangential momentum accommodation in the CLL model can be examined. Figs. 9c and 9d show the low incident angle and high incident angle scattering kernels associated with model #7, respectively. Note that $\sigma_n = 0.8$ for model #7, which corresponds to $\alpha_n = 0.96$ based on Eq. (6). It is clear that model #7 produces more quasi-specular scattering given that the associated scattering angular distributions are narrower than for diffuse scattering. At high incidence angles, model #7 produces sub-specular scattering as shown in Fig. 9d, where the angle of reflection is less than the angle of incidence. It is also helpful to consider the average energy accommodation assumed with model #7. For the CLL model, tangential energy accommodation is related to tangential momentum accommodation through the following expression (Cercignani & Lampis, 1971):

$$\alpha_t = \sigma_t(2 - \sigma_t) \tag{7}$$

Thus, for model #7, $\alpha_t = 0.96$. Since α_t and α_n are equivalent for this model, the average energy accommodation is nearly complete at 0.96. Model #7, a quasi-specular CLL model with incomplete momentum accommodation and near complete energy accommodation, appears to work well in helium-rich conditions based on ΔR proximity to zero in the right-most bin of Fig. 8.

The scattering kernels for the GSI assumptions in model #8 at low and high incident angles are shown in Figs. 9e and 9f, respectively. Model #8 produces nearly consistent inter-satellite density comparisons across the atmospheric He/O conditions sampled in this study. The scattering kernel differences from model #7 to model #8 include: 1) the low-incident angle reemission distribution narrows, and 2) the high-incident angle reemission distribution widens. This means that, for an elongated satellite like GRACE, scattering on the front plate is closer to specular while scattering on the side plates is closer to diffuse for model #8 in comparison to model #7. The normal and tangential momentum accommodation parameters in model #8 correspond to energy accommodation components of $\alpha_n = 0.75$ and $\alpha_t = 0.99$. For GRACE, this means that energy accommodation on the front plate is 0.75, while energy accommodation on the side plates is 0.99. To obtain an estimate of the average energy accommodation in model #8 for GRACE, the authors considered the force contribution of the side panels relative to the front panel in the same manner as was computed in Section 2.1 to obtain Fig. 2. Given that, on average, $\frac{C_D A_{sides}}{C_D A_{front}}$ for GRACE using model #8 is ∼0.35, the average energy accommodation for GRACE can then be estimated as $\alpha = 0.35\alpha_t + 0.65\alpha_n = 0.834$. Thus, average energy accommodation is smaller for model #8 than for model #7.

Figs. 9g and 9h show low and high incident angle scattering kernels, respectively, for model #9 which assumes significantly lower momentum accommodation. Normal and tangential energy accommodation for model #9 are both equal to 0.75, meaning the average energy accommodation for this model is 0.75. For model #9, scattering is closer to specular with a narrower angular distribution for both low and high incident angle interactions as compared to models #7 and #8. It makes sense, then, that model #9 produces ΔR results that approach those produced by a fully specular C_D model (model #11). The density discrepancy results then indicate that model #9 assumes energy and momentum accommodation that is too low, meaning that it is not an appropriate model at GRACE altitudes.

Some limitations should be discussed regarding the interpretation of ΔR across atmospheric He/O conditions. The examination of Fig. 8 reveals that it is harder to distinguish differences between C_D models at high He/O than at low He/O. Differences in ΔR between models #1-11 are smaller in the right-most bin of Fig. 8. This is one rea-

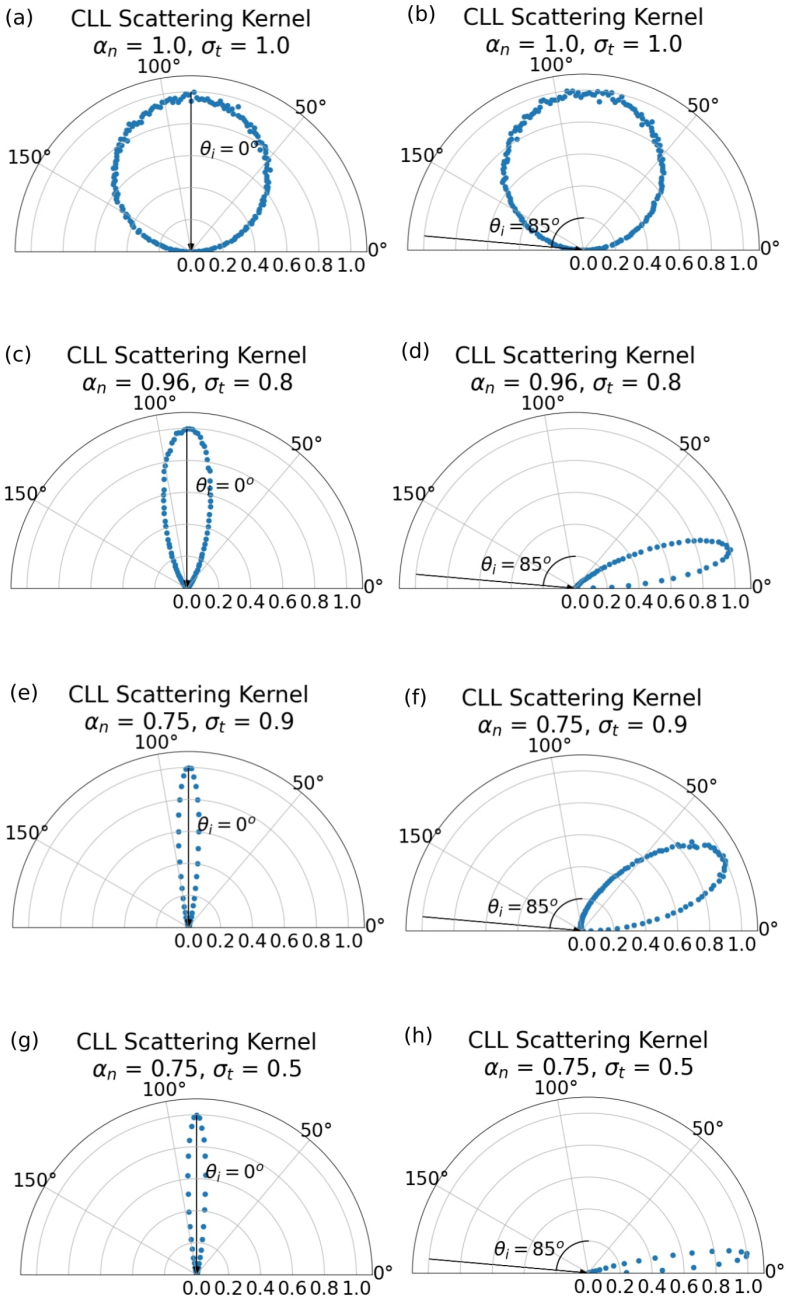

Figure 9. CLL angular probability distributions of reemitted particles assuming the GSI characteristics of model #3 at an incident angle of 0° (a), model #3 at an incident angle of 85° (b), model #7 at an incident angle of 0° (c), model #7 at an incident angle of 85° (d), model #8 at an incident angle of 0° (e), model #8 at an incident angle of 85° (f), model #9 at an incident angle of 0° (g), and model #9 at an incident angle of 85° (h)

son why it is important to consider how to quantify the uncertainty associated with each of these measurements. Table 5 compares different error metrics for each of the C_D models for the largest He/O bin alongside the measured ΔR range across the atmospheric He/O bins. The column titled 'ΔR measurement uncertainty from TLEs' includes ΔR uncertainty from TLE error estimates for the compact satellites. The TLE error estimates come from the TLE error model presented by Bernstein et al. (2021), which is a function of the satellite observed density. These TLE error estimates are then linearly propagated to the ΔR function. The column titled 'Robustness Range' alternatively presents the range in measured ΔR associated with removing any single compact satellite from the analysis. These uncertainty estimates provide a sense of how much the ΔR measurements could change given any of the compact satellites are removed from the analysis. The column titled 'RMSE' indicates the root mean squared error associated with the density ratio altitude fits based on the binned compact satellite observed densities for each C_D model. These RMSE estimates are the vertical error bars shown for each ΔR measurement in Fig. 8. In comparison to each of these ΔR error metrics, the range in ΔR measured for each C_D model across the atmospheric He/O bins is also shown in Table 5. These values are of similar magnitude compared to each of the error metrics, which makes it difficult to comprehensively quantify the effect of increased helium in the atmosphere.

Table 5. ΔR Error Metrics

C_D model	ΔR measurement uncertainty from TLEs	Robustness Range	RMSE	ΔR Range
Schamberg Diffuse, α=1.0, $\nu \to \infty$, $\phi_0 = 90°$	0.037	0.021	0.060	0.063
Sentman Diffuse, SESAM α	0.031	0.022	0.045	0.061
Sentman Diffuse, α=1.0	0.037	0.024	0.060	0.044
Sentman Diffuse, α=0.93	0.036	0.027	0.055	0.041
Sentman Diffuse, α=0.85	0.035	0.027	0.053	0.040
Sentman Diffuse, α=0.6	0.033	0.027	0.049	0.038
CLL QS, σ_n=0.8, σ_t=0.8	0.037	0.025	0.060	0.038
CLL QS, σ_n=0.5, σ_t=0.9	0.034	0.023	0.051	0.031
CLL QS, σ_n=0.5, σ_t=0.5	0.038	0.027	0.061	0.030
CLL QS, σ_n=0.9, σ_t=0.1	0.050	0.038	0.099	0.032
Schamberg Specular, $\alpha = 0.0$, $\nu = 1$, $\phi_0 = 0°$	0.039	0.029	0.064	0.020

4.1 Drag Coefficient, Density, and Orbit Propagation Error Exercise

Standard, widely-used C_D models in research and operational applications typically assume diffuse gas-surface interactions with complete or incomplete accommodation. The density discrepancy results shown in Fig. 8 indicate that diffuse and DRIA models are insufficient at GRACE altitudes near the oxygen-to-helium transition region. A quasi-specular C_D model with incomplete energy and momentum accommodation, like model #8, may be more suitable in this orbital regime given that it produces more consistent inter-satellite density comparisons. Considering model #8 to be a reasonable truth model in this orbital regime, errors in C_D and consequently derived density caused by making the standard assumption of diffuse scattering can be examined.

Fig. 10 compares C_D model #3 (Sentman diffuse with $\alpha = 1.0$) and C_D model #8 (CLL QS with $\sigma_n = 0.5$ and $\sigma_t = 0.9$) for GRACE over the course of ∼5 hours during the 120th day of the year in 2003. During this time period, using the Sentman diffuse C_D model instead of the quasi-specular CLL C_D model would result in derived density errors of ∼25%. In 2009 during solar minimum conditions, implementing the Sentman diffuse C_D model would yield similar derived density errors of ∼27%.

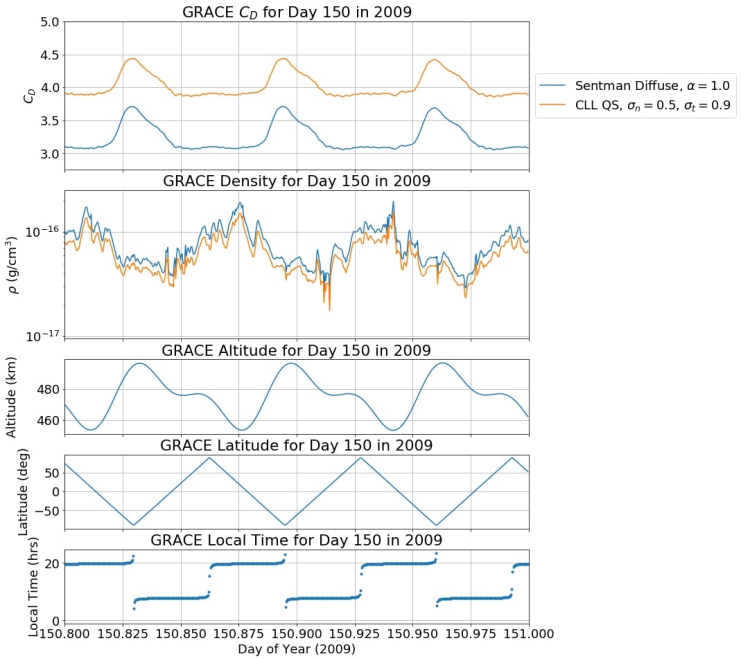

Figure 10. GRACE C_D (1st panel), derived density (2nd panel), altitude (3rd panel), latitude (4th panel), and local time (5th panel) are shown over the course of ∼5 hours on day 120 in the year 2003.

Table 6. Example Orbit Propagation Maximum In-Track Differences

Date	24hr In-Track Difference (m)	72hr In-Track Difference (m)
2009, DOY 150	31	64
2003, DOY 120	341	380

It is also helpful to consider potential orbit propagation effects associated with using different C_D models. The authors performed a simple exercise to examine the C_D effect on orbit propagation for GRACE in solar maximum and solar minimum conditions. GRACE position and velocity were integrated and MSIS model density was used to propagate the orbit of GRACE over 24-hour and 72-hour time periods, using each of the 11 C_D models examined in this study. At the end of the 24-hour and 72-hour integration time periods, the authors examined the in-track differences for GRACE. Results of this exercise are summarized in Table 6. In solar minimum conditions (day 150, year 2009), the maximum in-track difference across the 24-hour orbit propagation runs for each of the 11 different C_D models was 31 meters. This value approximately doubled to 64 meters after 72-hours. In solar maximum conditions (day 120, year 2003), the in-track differences increased by an order of magnitude to ∼300-400 meters for both the 24-hour and 72-hour orbit integration runs. It should be noted that solar maximum in-track differences were more variable and could change significantly if the authors chose a different starting day. However, maximum in-track differences typically were on the order of hundreds of meters in 2003. This exercise suggests that the divergence of C_D models at GRACE altitudes could lead to orbital in-track errors of tens to hundreds of meters depending on the level of solar activity.

5 Discussion

The results presented in this paper provide evidence to support the implementation of a gas-surface interaction model which assumes quasi-specular scattering with incomplete energy and momentum accommodation at altitudes near ∼500 km. This is the orbital regime where the oxygen-to-helium transition region emerges. This result marks a significant shift from the standard assumption of diffuse scattering in LEO orbital conditions, an assumption that is rooted in measurements from lower altitudes (<350 km).

Based on the ΔR analysis, the GSI models that implement quasi-specular gas-surface interactions produce the most consistent densities between GRACE and the compact satellites. These results are novel for on-orbit GSI in the context of widely used DRIA models. For the elongated GRACE satellite, diffuse models produce C_D values that are too low, while specular or near-specular models produce C_D values that are too high. Models #7 and #8 yield ΔR values closest to zero depending on the average atmospheric He/O, though the optimal model implementation could take a variety of different forms. Both low-incident angle and high-incident angle gas-surface interactions drive the density consistency results. As helium increases in the atmosphere, high-incident angle interactions become more important.

It is important to discuss potential limitations of this study that may impact the density consistency results. Most of the compact satellites used in this study have moderately elliptical orbits in contrast to the nearly circular orbit of GRACE. It is possible that there may be a suborbital time dependence or perigee velocity dependence in the physical drag coefficient for the compact satellites. In this scenario, optimal GSI models may need to incorporate differences in scattering based on incident velocity. There may be different adsorption characteristics associated with compact object circular orbits compared to elliptical orbits. Objects with elliptical orbits have greater perigee velocities than objects with circular orbits, which means that atmospheric molecules strike the elliptical orbit satellites with greater kinetic energy. This may mean that energy accommodation is smaller, and atomic oxygen molecules are less likely to adsorb to the surface of an elliptical orbit object at perigee (K. Moe & Moe, 2005; Pilinski et al., 2013). Examination of this potential effect on ΔR is beyond the scope of this paper.

An additional limitation of this study is the use of MSIS for atmospheric inputs to the C_D models. Helium-rich atmospheric conditions and helium-related uncertainties in the C_D models at upper thermospheric altitudes are of particular interest to the authors. These are the regimes that tend to be the most uncertain in empirical models like MSIS. This highlights the circular nature of this problem, wherein the authors are attempting to validate appropriate physical C_D assumptions in order to estimate and mitigate C_D-related biases at upper thermospheric altitudes, but the C_D models themselves depend on modeled upper atmospheric constituents which may carry the same uncertainties and biases. If helium is wrong in MSIS, the C_D model will also assume the wrong amount of helium.

Additionally, it is important to note that there are multiple theoretical solutions which may exist that could yield inter-satellite density consistency. The authors have discussed two potential CLL models that work well in varying atmospheric He/O conditions based on ΔR proximity to zero. To better constrain all possible solutions for optimal GSI parameters, the authors plan to leverage laboratory scattering data. One way to do this might be to fit CLL scattering parameters to laboratory scattering data for He and O using DSMC-generated scattering kernels, like the ones shown in Fig. 9.

The density discrepancy analysis could also be enriched by incorporating additional datasets in this analysis. Including densities from the Swarm satellites would be a way to sample higher altitude orbital conditions. Swarm B has an orbital altitude of ∼530 km, which is slightly higher that the orbital altitude of GRACE, and Swarm densities

have been derived from GPS data instead of accelerometers (March, Doornbos, & Visser, 2019). With higher altitudes, Swarm B is likely to sample more helium-rich atmospheric conditions than GRACE. Additionally, the Swarm satellites were launched in 2013, which means they provide data covering the most recent solar cycle. The GRACE density data analyzed in this study covers the years 2002 - 2010. Sampling years post-2013 also opens the possibility of including more compact satellites with more recent launch dates.

This analysis might also be expanded by including comparisons between satellites with different orientations for which the appropriate scattering scenarios might be more clearly emphasized. This could include data where Swarm A and C, orbiting at ∼470 km, have different attitudes. Planet Labs Flock 1-C CubeSats could also provide data for these comparisons, as these satellites have low-drag and high-drag control modes (Foster et al., 2015). These modes correspond to orientations parallel to the flow and perpendicular to the flow, respectively. Scattering comparisons between satellites with different attitudes would be helpful for evaluting C_D model assumptions related to incident angle, given that such satellites fly through the same atmosphere but may have very different levels of low-incidence and high-incidence scattering.

The inter-satellite density consistency results presented here provide a novel contribution to GSI modeling efforts in the upper thermosphere. This orbital regime is host to a growing number of resident space objects and is where physical C_D models tend to diverge due to uncertainty in model assumptions. With this work the authors have been able to constrain GSI assumptions at ∼500 km to quasi-specular with incomplete energy and momentum accommodation, providing evidence that both diffuse and specular scattering assumptions are inappropriate at these altitudes.

Appendix A Bates Profile Fitting

Altitude differences between GRACE and some of the compact satellites can lead to differences in measured-to-modeled density ratios. The authors implemented a least-squares fitting scheme to fit the altitude structure of measured-to-modeled density ratios for the compact satellites to the ratio of two Bates profiles (Bates, 1959). The purpose of obtaining a physically-informed vertical profile of measured-to-modeled density ratio for the compact satellites was to be able to attain a value for $\frac{\rho_{obs}}{\rho_{mod}}$ for a spherical satellite at the precise location of GRACE. This value comes from the fitted density ratio profile, which is constructed using data from each of the compact satellites.

The observed-to-modeled density ratio fits are constructed based on the assumption that exospheric temperature differences are causing the offset between the observed and modeled densities. As such, the ratio of two Bates profiles is fit to the observed-to-modeled density ratios for the compact satellites, where the the two profiles have different exospheric temperatures. The ratio of two Bates profiles is chosen as the parametric equation to fit to the density ratio data because the Bates temperature profile is considered to be a physically consistent representation of temperature in the middle and upper thermosphere, including above the turbopause in diffusive equilibrium. Also, the MSIS model is constructed based on Bates profiles (Picone et al., 2002). In this region of diffusive equilibrium, where each of the satellites in this analysis reside, integration of the species vertical hydrostatic balance equation for a Bates temperature profile gives the number density of a constituent in diffusive equilibrium (Chamberlain & Hunten, 1987; Picone et al., 2013):

$$n_i(\zeta) = n_{i,\ell} \left[\frac{T_\ell}{T(\zeta)} \right]^{1+\gamma_i+\alpha_i} \exp\left(-\gamma_i \sigma(\zeta - \zeta_\ell)\right) \tag{A1}$$

where ζ is the geopotential altitude, i is the index for each species constituent, and the subscript ℓ indicates the lower boundary of the diffusive equilibrium region. The geometric altitude of this lower boundary is often chosen to be 120 km. Picone et al. (2016)

point out that the region between ∼100 km and ∼200 km should be considered a transition region such that ∼200 km marks the lower boundary of the diffusive equilibrium region. For this study, the authors choose 150 km as the geometric altitude of the lower boundary of the diffusive equilibrium region. The inverse temperature scale height σ is given as:

$$\sigma = \frac{T_\ell^{'}}{T_\infty - T_\ell} \tag{A2}$$

where $T_\ell^{'}$ is the vertical temperature gradient at the reference lower boundary altitude. The ratio γ_i of temperature and species scale heights is given as:

$$\gamma_i = \frac{1}{\sigma H_{i,\infty}} \tag{A3}$$

where H signifies scale height. The species thermal diffusion coefficient α_i is given as (Picone et al., 2002, 2013):

$$\alpha_i = \begin{cases} -0.38 & \text{for He and H} \\ 0.0 & \text{for O, } O_2\text{, and } N_2 \end{cases} \tag{A4}$$

Then a parametric fitting equation can be written for the ratio of two Bates profiles; an 'observed' profile signified by the superscript A and a 'modeled' profile signified by the superscript B:

$$\frac{n_i^A}{n_i^B} = \frac{n_{i,\ell}^A}{n_{i,\ell}^B} T_\ell^{\left(\frac{1}{\sigma^A H_{i,\infty}^A} - \frac{1}{\sigma^B H_{i,\infty}^B}\right)} \frac{T_\infty^{B\left(1+\frac{1}{\sigma^B H_{i,\infty}^B}+\alpha_i\right)}}{T_\infty^{A\left(1+\frac{1}{\sigma^A H_{i,\infty}^A}+\alpha_i\right)}} \exp\left[\left(\frac{1}{H_{i,\infty}^B} - \frac{1}{H_{i,\infty}^A}\right)(\zeta - \zeta_\ell)\right] \tag{A5}$$

In Eq. (A5), exospheric temperature T_∞ has replaced $T(\zeta)$ due to the isothermal nature of this region, and Eq. (A3) has been plugged into Eq. (A1) for both A and B profiles. Additionally, the temperature at the lower boundary T_ℓ is assumed to be the same for both the A and B profiles.

Eq. (A5) applies to each individual thermospheric constituent species. To maintain a reasonable number of parameters to fit, the authors assume the thermosphere is composed primarily of O and He at the satellite altitudes of interest. Then the system of equations to fit to the data becomes:

$$\begin{cases} \frac{n_O^A}{n_O^B} = \frac{n_{O,\ell}^A}{n_{O,\ell}^B} T_\ell^{\left(\frac{1}{\sigma^A H_{O,\infty}^A} - \frac{1}{\sigma^B H_{O,\infty}^B}\right)} \frac{T_\infty^{B\left(1+\frac{1}{\sigma^B H_{O,\infty}^B}+\alpha_O\right)}}{T_\infty^{A\left(1+\frac{1}{\sigma^A H_{O,\infty}^A}+\alpha_O\right)}} \exp\left[\left(\frac{1}{H_{O,\infty}^B} - \frac{1}{H_{O,\infty}^A}\right)(\zeta - \zeta_\ell)\right] \\ \frac{n_{He}^A}{n_{He}^B} = \frac{n_{He,\ell}^A}{n_{He,\ell}^B} T_\ell^{\left(\frac{1}{\sigma^A H_{He,\infty}^A} - \frac{1}{\sigma^B H_{He,\infty}^B}\right)} \frac{T_\infty^{B\left(1+\frac{1}{\sigma^B H_{He,\infty}^B}+\alpha_{He}\right)}}{T_\infty^{A\left(1+\frac{1}{\sigma^A H_{He,\infty}^A}+\alpha_{He}\right)}} \exp\left[\left(\frac{1}{H_{He,\infty}^B} - \frac{1}{H_{He,\infty}^A}\right)(\zeta - \zeta_\ell)\right] \\ \frac{\rho^A}{\rho^B} = \frac{\sum m_i n_i^A}{\sum m_i n_i^B} = \frac{\frac{n_O^A}{n_O^B}(n_O^B m_O) + \frac{n_{He}^A}{n_{He}^B}(n_{He}^B m_{He})}{n_O^B m_O + n_{He}^B m_{He}} \end{cases} \tag{A6}$$

Model output from MSIS is leveraged to reduce the number of unknown parameters in Eq. (A6). Since B represents 'modeled' values, and the temperature at the lower boundary is assumed to be the same for the 'observed' and 'modeled' profiles, MSIS is used to obtain values for n_O^B, n_{He}^B, T_ℓ, $T_\ell^{'}$, and T_∞^B. The MSIS runs used to obtain these values were selected to represent the observed atmospheric conditions based on the F10.7 and Ap inputs used to initiate the model runs. Then, plugging in the MSIS-modeled parameters and known constants (including the masses of atomic oxygen and helium), this leaves three unknown parameters to fit:

$$\begin{cases} C_1 = \frac{n_{O,\ell}^A}{n_{O,\ell}^B} \\ C_2 = \frac{n_{He,\ell}^A}{n_{He,\ell}^B} \\ C_3 = T_\infty^A \end{cases} \tag{A7}$$

The authors perform non-linear least squares fitting of Eq. (A6) to the $\frac{\rho_{obs}}{\rho_{mod}}$ data for the compact satellites.

Note that the parametric expression in Eq. (A6) is a function of geopotential altitude. In order to make the density ratio data a function of geopotential altitude, derived densities were converted into corresponding geopotential altitudes by interpolating to the MSIS profiles used to obtain some of the parameter estimates in Eq. (A6).

Acknowledgments

The Two-Line Element data used to compute integrated densities from orbital changes for the selected set of compact satellites are available at Space-Track.org via `https://www.space-track.org/#gp` with account registration required. The accelerometer-derived density datasets for the GRACE A and B satellites are provided by P. M. Mehta and E. K. Sutton at `http://tinyurl.com/densitysets`, courtesy of P. M. Mehta et al. (2017). MSIS simulations used in this work are obtained from the model downloaded from `https://gitlab.com/afedynitch/Python-NRLMSISE-00`. Drag coefficient simulations in this study were completed using the Vehicle Environment Coupling and TrajectOry Response (VECTOR) software, which can be downloaded at `https://github.com/SWxTREC/vector-code`.

This material is based upon work supported in part by the National Science Foundation Graduate Research Fellowship under Grant No. 1650115. Dr. Pilinski is supported by NASA Grant No. 80NSSC19K0492.

References

Bates, D. R. (1959). Some problems concerning the terrestrial atmosphere above about the 100 km level. *Proceedings of the Royal Society of London. Series A. Mathematical and Physical Sciences*, *253*(1275), 451–462. doi: 10.1098/rspa.1959.0207

Beletskii, V. (1970). Interaction of the aerodynamic stream with a satellite according to an analysis of the motion of "proton-2" about its center of mass. *Cosmic Research*, *8*, 189.

Bernstein, V., Pilinski, M., & Knipp, D. (2020). Evidence for drag coefficient modeling errors near and above the oxygen-to-helium transition. *Journal of Spacecraft and Rockets*, *57*(6), 1246–1263. doi: 10.2514/1.A34740

Bernstein, V., Pilinski, M., & Sutton, E. K. (2021). Assessing thermospheric densities derived from orbital drag data. In *Proceedings of the 31st aas/aiaa space flight mechanics meeting*. AAS Publications Office.

Bouwer, S. (1992). Periodicities of solar irradiance and solar activity indices, ii. *Solar Physics*, *142*(2), 365–389. doi: 10.1007/BF00151460

Bowman, B., & Moe, K. (2005). Drag coefficient variability at 175-500km from the orbit decay analyses of spheres. In *Aas/aiaa astrodynamics specialist conference.*

Carter, V. L., Ching, B. K., & Elliott, D. D. (1969). Atmospheric density above 158 kilometers inferred from magnetron and drag data from the satellite ov1-15 (1968-059a). *Journal of Geophysical Research*, *74*(21), 5083–5091. doi: 10.1029/JA074i021p05083

Cercignani, C., & Lampis, M. (1971). Kinetic models for gas-surface interactions. *Transport Theory and Statistical Physics*, *1*(2), 101–114. doi: 10.1080/00411457108231440

Cercignani, C., & Lampis, M. (1997). New scattering kernel for gas-surface interaction. *AIAA journal*, *35*(6), 1000–1011. doi: 10.2514/2.209

Chamberlain, T. P., & Hunten, D. M. (1987). *Theory of planetary atmospheres: an introduction to their physics and chemistry*. Academic Press, Inc., New York.

Ching, B., Hickman, D., & Straus, J. (1977). Effects of atmospheric winds and aerodynamic lift on the inclination of the orbit of the s3-1 satellite. *Journal of Geophysical Research*, *82*(10), 1474–1480. Retrieved from `https://agupubs.onlinelibrary.wiley.com/doi/abs/10.1029/JA082i010p01474` doi: 10.1029/JA082i010p01474

Cook, G. (1965). Satellite drag coefficients. *Planetary and Space Science*, *13*(10), 929–946. doi: 10.1016/0032-0633(65)90150-9

Crisp, N., Roberts, P., Livadiotti, S., Rojas, A. M., Oiko, V., Edmondson, S., ... others (2021). In-orbit aerodynamic coefficient measurements using soar (satellite for orbital aerodynamics research). *Acta Astronautica*, *180*, 85–99. Retrieved from `https://www.sciencedirect.com/science/article/pii/S0094576520307591` doi: https://doi.org/10.1016/j.actaastro.2020.12.024

Doornbos, E. (2012). *Thermospheric density and wind determination from satellite dynamics*. Springer Science & Business Media, Heidelberg, Germany. doi: 10.1007/978-3-642-25129-0

Emmert, J. (2009). A long-term data set of globally averaged thermospheric total mass density. *Journal of Geophysical Research: Space Physics*, *114*(A6). doi: 10.1029/2009JA014102

Foster, C., Hallam, H., & Mason, J. (2015). Orbit determination and differential-drag control of planet labs cubesat constellations. In *Proceedings of the aiaa astrodynamics specialist conference.*

Gaposchkin, E. M. (1994). *Calculation of satellite drag coefficients* (Tech. Rep. No. 998). Massachusetts Institute Of Technology Lincoln Laboratory.

Goodman, F. O., & Wachman, H. Y. (1967). Formula for thermal accommodation coefficients. *The Journal of Chemical Physics*, *46*(6), 2376–2386. doi: 10.1063/1.1841046

Gregory, J. C., & Peters, P. N. (June 1986). A measurement of the angular distribution of 5 ev atomic oxygen scattered off a solid surface in earth orbit. In *Proceedings of the 15th international symposium on rarefied gas dynamics* (pp. 644–654). Stuttgart: B. G. Teubner, Germany.

Harrison, I., & Swinerd, G. (1996). A free molecule aerodynamic investigation using multiple satellite analysis. *Planetary and space science*, *44*(2), 171–180. doi: 10.1016/0032-0633(95)00077-1

Hedin, A. E., Hinton, B. B., & Schmitt, G. A. (1973). Role of gas-surface interactions in the reduction of ogo 6 neutral particle mass spectrometer data. *Journal of Geophysical Research*, *78*(22), 4651–4668. doi: 10.1029/JA078i022p04651

Imbro, D. R., Moe, M. M., & Moe, K. (1975). On fundamental problems in the deduction of atmospheric densities from satellite drag. *Journal of Geophysical Research*, *80*(22), 3077–3086. doi: 10.1029/JA080i022p03077

Liu, S.-M., Sharma, F. K., & Knuth, E. L. (1979). Satellite drag coefficients calculated from measured distributions of reflected helium atoms. *AIAA Journal*, *17*(12), 1314–1319. doi: 10.2514/3.7629

Lord, R. (1991). Some extensions to the cercignani-lampis gas-surface scattering kernel. *Physics of Fluids A: Fluid Dynamics*, *3*(4), 706–710. doi: 10.1063/1.858076

March, G., Doornbos, E. N., & Visser, P. (2019). High-fidelity geometry models for improving the consistency of champ, grace, goce and swarm thermospheric density data sets. *Advances in Space Research*, *63*(1), 213–238. doi: 10.1016/j.asr.2018.07.009

March, G., van den IJssel, J., Siemes, C., Visser, P. N., Doornbos, E. N., & Pilinski, M. (2021). Gas-surface interactions modelling influence on satellite aerodynamics and thermosphere mass density. *Journal of Space Weather and Space Climate*, *11*, 54. doi: 10.1051/swsc/2021035

March, G., Visser, T., Visser, P., & Doornbos, E. N. (2019). Champ and goce

thermospheric wind characterization with improved gas-surface interactions modelling. *Advances in Space Research*, *64*(6), 1225–1242. doi: 10.1016/j.asr.2019.06.023

Mehta, N. A., Murray, V. J., Xu, C., Levin, D. A., & Minton, T. K. (2018). Non-reactive scattering of n2 from layered graphene using molecular beam experiments and molecular dynamics. *The Journal of Physical Chemistry C*, *122*(18), 9859–9874. doi: 10.1021/acs.jpcc.7b11721

Mehta, P. M., Walker, A., Lawrence, E., Linares, R., Higdon, D., & Koller, J. (2014). Modeling satellite drag coefficients with response surfaces. *Advances in Space Research*, *54*(8), 1590–1607. doi: 10.1016/j.asr.2014.06.033

Mehta, P. M., Walker, A. C., Sutton, E. K., & Godinez, H. C. (2017). New density estimates derived using accelerometers on board the champ and grace satellites. *Space Weather*, *15*(4), 558–576. doi: 10.1002/2016SW001562

Minton, T. K., Tagawa, M., & Nathanson, G. M. (2004). Energy accommodation in hyperthermal gas-surface collisions: Aerobraking in planetary atmospheres. *Journal of Spacecraft and Rockets*, *41*(3), 389–396. doi: 10.2514/1.10724

Moe, K. (1966). Absolute atmospheric densities determined from the spin and orbital decays of explorer vi. *Planetary and Space Science*, *14*(11), 1065–1075. doi: 10.1016/0032-0633(66)90022-5

Moe, K., & Bowman, B. (2005). The effects of surface composition and treatment on drag coefficients of spherical satellites. In *Proceedings of the aas/aiaa astrodynamics specialists conference.* American Astronautical Society Publications Office, San Diego, CA.

Moe, K., & Moe, M. M. (1992). The deduction of in-track winds from satellite measurements of density and composition. *Geophysical Research Letters*, *19*(13), 1343–1346. doi: 10.1029/92GL01114

Moe, K., & Moe, M. M. (2005). Gas-surface interactions and satellite drag coefficients. *Planetary and Space Science*, *53*(8), 793–801. doi: 10.1016/j.pss.2005.03.005

Moe, K., Moe, M. M., & Yelaca, N. W. (1972). Effect of surface heterogeneity on the adsorptive behavior of orbiting pressure gages. *Journal of Geophysical Research*, *77*(22), 4242–4247. doi: 10.1029/JA077i022p04242

Moe, M. M., Wallace, S. D., & Moe, K. (1993). Refinements in determining satellite drag coefficients: Method for resolving density discrepancies. *Journal of Guidance, Control, and Dynamics*, *16*(3), 441–445. doi: 10.2514/3.21029

Moe, M. M., Wallace, S. D., & Moe, K. (1995). Recommended drag coefficients for aeronomic satellites. *The Upper Mesosphere and Lower Thermosphere: A Review of Experiment and Theory, Geophysical Monograph Series*, *87*, 349–356. doi: 10.1029/GM087p0349

Murray, V. J., Pilinski, M. D., Smoll Jr, E. J., Qian, M., Minton, T. K., Madzunkov, S. M., & Darrach, M. R. (2017). Gas-surface scattering dynamics applied to concentration of gases for mass spectrometry in tenuous atmospheres. *The Journal of Physical Chemistry C*, *121*(14), 7903–7922. doi: 10.1021/acs.jpcc.7b00456

Nayar, S. P. (2006). Periodicities in solar activity and their signature in the terrestrial environment. In N. Gopalswamy & A. Bhattacharyya (Eds.), *Proceedings of the ilws workshop "the solar influence on the heliosphere and earth's environment: Recent progress and prospects", goa* (pp. 170–178).

Pardini, C., Anselmo, L., Moe, K., & Moe, M. M. (2009). Drag and energy accommodation coefficients during sunspot maximum. *Advances in Space Research*, *45*(5), 638–650. doi: 10.1016/j.asr.2009.08.034

Picone, J., Emmert, J., & Drob, D. (2016). Consistent static models of local thermospheric composition profiles. *arXiv preprint arXiv:1607.03370 [physics.space-ph]*.

Picone, J., Emmert, J., & Lean, J. (2005). Thermospheric densities derived from

spacecraft orbits: Accurate processing of two-line element sets. *Journal of Geophysical Research: Space Physics*, *110*(A3). doi: 10.1029/2004JA010585

Picone, J., Hedin, A., Drob, D. P., & Aikin, A. (2002). Nrlmsise-00 empirical model of the atmosphere: Statistical comparisons and scientific issues. *Journal of Geophysical Research: Space Physics*, *107*(A12), 1-16. doi: 10.1029/2002JA009430

Picone, J., Meier, R., & Emmert, J. (2013). Theoretical tools for studies of low-frequency thermospheric variability. *Journal of Geophysical Research: Space Physics*, *118*(9), 5853–5873. doi: 10.1002/jgra.50472

Pilinski, M. D., Argrow, B. M., & Palo, S. E. (2011). Drag coefficients of satellites with concave geometries: Comparing models and observations. *Journal of Spacecraft and Rockets*, *48*(2), 312–325. doi: 10.2514/1.50915

Pilinski, M. D., Argrow, B. M., Palo, S. E., & Bowman, B. R. (2013). Semi-empirical satellite accommodation model for spherical and randomly tumbling objects. *Journal of Spacecraft and Rockets*, *50*(3), 556–571. doi: 10.2514/1.A32348

Poovathingal, S. J., Xu, C., Murray, V., Minton, T. K., & Schwartzentruber, T. E. (2019). Gas-surface model in dsmc for molecules passing through a funnel-type gas concentrator. In *Aiaa scitech 2019 forum.* doi: 10.2514/6.2019-1281

Qian, L., Burns, A. G., Emery, B. A., Foster, B., Lu, G., Maute, A., ... Wang, W. (2014). The ncar tie-gcm: A community model of the coupled thermosphere/ionosphere system. *Modeling the Ionosphere-Thermosphere System*, *201*, 73–83. doi: 10.1002/9781118704417.ch7

Schaaf, S., & Chambre, P. (1958). Flow of rarefied gases, high speed aerodynamics and jet propulsion. In H. W. Emmons (Ed.), *Fundamentals of gas dynamics* (Vol. 3, pp. 687–741). Princeton University Press, Princeton, NJ.

Schamberg, R. (1959). *A new analytic representation of surface interaction for hyperthermal free molecular flow with applications to neutral-particle drag estimates of satellites* (Tech. Rep. No. RM-2313). Rand Corporation, Santa Monica, CA.

Seidl, M., & Steinheil, E. (1974). Measurements of momentum accommodation coefficients on surfaces characterized by auger spectroscopy, sims and leed. In M. Becker & M. Fiebig (Eds.), *Proceedings of the ninth international symposium on rarefied gas dynamics.* DFVLR-Press, Porz-Whan.

Sentman, L. H. (1961). *Free molecule flow theory and its application to the determination of aerodynamic forces* (Tech. Rep. No. LMSC-448514). Lockheed Missiles and Space Co. Inc., Sunnyvale, CA.

Storch, J. (2002). *Aerodynamic disturbances on spacecraft in free-molecular flow* (Tech. Rep. No. TR-2003(3397)-l). The Aerospace Corporation, Vehicle Systems Division, El Segundo, CA.

Sutton, E. K., Nerem, R. S., & Forbes, J. M. (2007). Density and winds in the thermosphere deduced from accelerometer data. *Journal of Spacecraft and Rockets*, *44*(6), 1210–1219. doi: 10.2514/1.28641

Turansky, C. P. (2012). *High-fidelity dynamic modeling of spacecraft in the continuum–rarefied transition regime* (Unpublished doctoral dissertation). University of Colorado at Boulder.

Virgili, J., & Roberts, P. C. (2013). δdsat, a qb50 cubesat mission to study rarefied-gas drag modelling. *Acta Astronautica*, *89*, 130–138. doi: 10.1016/j.actaastro.2013.04.006

Wachman, H. Y. (1962). The thermal accommodation coefficient: A critical survey. *American Rocket Society Journal*, *32*(1), 2–12. doi: 10.2514/8.5939

Walker, A., Mehta, P., & Koller, J. (2014). Drag coefficient model using the cercignani-lampis-lord gas-surface interaction model. *Journal of Spacecraft and Rockets*, *51*(5), 1544–1563. doi: 10.2514/1.A32677